Combining Multispectral and Three-Dimensional Data From Drone Imagery to Detect Forest Insect Damage: an Evaluation of a Novel Approach to Identify the Vertical Structure of Damage in Trees in the Northern Rocky Mountains, USA

A Thesis

Presented in Partial Fulfillment of the Requirements for the

Degree of Master of Science

with a

Major in Geography

in the

College of Graduate Studies

University of Idaho

by

Abhinav Shrestha

Approved by:

Major Professor: Jeffrey A. Hickey, Ph.D.

Committee Members: Jason W. Karl, Ph.D.; Arjan J.H. Meddens, Ph.D.

Department Administrator: Alistair Smith, Ph.D.

December 2023

Abstract

Remote sensing is a well-established tool for detecting forest disturbances. The increased availability of Uncrewed Aerial Systems (drones) and advances in computer algorithms have resulted in an increase in studies of forest insects using drones. To date, most studies have used height information from three-dimensional (3D) point clouds to segment individual trees and have used two-dimensional multispectral images to identify tree damage. Here, I describe a novel approach of classifying the multispectral reflectances of the 3D point cloud into damaged and healthy classes, retaining the height information for assessment of the vertical distribution of damage within a tree. Drone images were acquired in a study area in the Northern Rocky Mountains that experienced recent damage from insects and processed to produce a point cloud. A random forest (RF) classification model was developed from the multispectral data of these points, which had an overall accuracy (OA) of 98.6% and, when applied across the study area, classified 77% of the points with a confidence of greater than 75%. Based on these classified points and segmented trees, I developed and evaluated algorithms to separate healthy and damaged trees, and for damaged trees, identified multiple damage types based on percentages of red and gray points on each tree. Healthy and damaged trees were identified with high accuracy (OA: 93.5%), with most of the trees in the 27-ha study area classified as healthy (78.3%). The remaining damaged trees were separated into different damage types with moderate accuracy (OA: 70.1%). A subsequent algorithm identified top-kill with high accuracy (OA: 91.8%), with most damaged trees in the study area exhibiting top-kill (78.9%). Our results demonstrate the utility of drone data for monitoring the vertical structure of tree damage from forest insects and diseases.

Acknowledgments

First and foremost, I would like to express my sincere gratitude to my advisor, Dr. Jeffrey A. Hicke, for his unwavering support and guidance in helping me develop this project and thesis. Dr. Hicke's mentorship has significantly contributed to my academic and professional growth. His invaluable expertise in the field of climate change, insect outbreaks, remote sensing, and programming has helped develop my skills in executing effective scientific research and communication. Thank you to Dr. Jason W. Karl for serving as my MS thesis committee member and for introducing me to the world of drone-based remote sensing. Dr. Karl's excellent hands-on teaching methods and his enthusiastic support of my research inquiries have helped me develop this thesis from a conceptual idea to an applicable methodology. Thank you to Dr. Arjan J.H. Meddens for serving as my MS thesis committee member, providing me with insights and advice for my thesis, and for giving me the opportunity to work for the NASA Commercial SmallSat Data Acquisition (CSDA) project. The data used for this MS thesis was collected for the NASA CSDA project (award #80NSSC21K1155), therefore, I would like to thank the project members: Dr. Jeffrey A. Hicke (University of Idaho), Dr. Arjan Meddens (Washington State University (WSU)), Dr. Amanda Stahl (WSU), Luke Schefke (WSU), Dr. Andrew Hudak (US Forest Service (USFS)), and Benjamin Bright (USFS). Special thanks to Dr. Amanda Stahl for planning and executing the drone missions and for helping with processing the collected data. The research was conducted in the ancestral homelands of the Kootenai (Ksanka), Pend d'Oreille (Q̓lispé), and Salish (Sélish) tribes of western Montana. Finally, I am grateful to my peers Ian Woodruff and Caroline Ludwig for always being my sounding board, providing me with their insightful feedback, and enlightening me with their knowledge of the outdoors.

Dedication

To my mother, father, grandmother, and Kei. Thank you for your unconditional love and support.

In loving memory of my beloved grandfather, the inspiration for my scientific curiosity.

Table of Contents

Abstract ii

Acknowledgments iii

Dedication iv

Table of Contents v

List of Tables viii

List of Figures ix

1. Introduction 1

2. Methods 5

    2.1 Study area 5

    2.2 Drone imagery collection 7

    2.3 Drone imagery pre-processing 7

    2.4 Reference data 10

    2.5 Tree segmentation 11

        2.5.1 Ground and non-ground classification, and height-normalization of point cloud 11

        2.5.2 Point cloud segmentation into unique tree objects 11

    2.6 Point-level classification with random forest models 14

    2.7 Tree-level damage algorithm 16

    2.8 Characterization of the extent of tree damage across the UAV scene 18

3. Results 19

    3.1 Tree segmentation 19

    3.2 Point-level classification into health status classes 21

    3.3 Tree-level damage 26

    3.4 Tree damage across the study site 30

4. Discussion 36

5. Conclusion 40

References 42

Appendix A. Outbreak history of study area and drone mission flight lines 51

Appendix B: Drone data pre-processing 52

B.1. GCP marker corrections and point cloud optimization 52

B.2. Assignment of multispectral reflectance values to SfM point cloud 53

Appendix C. Reference data 54

C.1. Individual drone-captured images 54

C.2. On-screen selection of points representing green, grey, red, and shadow classes on the point cloud data set. 54

Appendix D. Segmentation of point cloud into trees 56

D.1. Ground classification and height normalization of point cloud 56

D.2. Tree segmentation algorithms 56

D.2.1. Algorithm background and parameters 56

D.2.2. Case study to compare tree segmentation algorithms 58

D.2.3. Accuracy assessment of tree segmentation 60

Appendix E. Correlation matrix of predictor variables used in RF models 62

Appendix F. Evaluation of point classification 63

Appendix G. Application of final RF model to point cloud 65

Appendix H. Tree-level damage algorithm 67

H.1. Definition of damage classes 67

H.2. Preparation of point cloud for damage assessment algorithm 68

H.3. Types of tree-level damage algorithms 69

H.4. Accuracy assessment of tree-level damage algorithm 70

H.5. Live crown base issue with SfM point clouds 73

List of Tables

Table 2.1. Name, equation, and reference for vegetation indices used in the project. ρ is reflectance. 14

Table 3.1. Confusion matrix and accuracy metrics of the accuracy assessment of the point cloud-based tree segmentation algorithm (Li et al., 2012). "*Tree segmentation issue*" refers to either the reference point (identified as a tree) falling in between crown segments of a single tree that were divided into multiple trees (over-segmentation) or the reference point (identified as on the ground or understory vegetation) falling within the erroneously delineated tree crown. "*Ground issue*" refers to the misclassification of understory or ground as trees. 20

Table 3.2. Confusion matrix and accuracy metrics of the final random forest model (RBI + NDVI + REDEDGE) for classifying points into healthy, damaged, and other classes. 24

Table 3.3. Confusion matrix and accuracy metrics for evaluation of algorithm to separate healthy trees from damaged trees. Results are averages from resampling (with replacement; 500 times) to address class imbalance. 27

Table 3.4. Confusion matrix and accuracy metrics for evaluation of algorithm to separate healthy trees and different types of tree damage. Results are averages from resampling (with replacement; 500 times) to address class imbalance. "OA": overall accuracy. 28

Table 3.5. Confusion matrix and accuracy metrics for evaluation of top-kill algorithm to separate "*top-kill*" and "*non-top-kill*" from the subset of "*damaged*" trees. Results are averages from resampling (with replacement; 100 times) to address class imbalance. 29

Table 3.6. Summary of tree-level metrics of healthy and damaged trees, and different damage types across the study site. "TK": top-kill. 31

List of Figures

Figure 2.1. Yellow polygons around the 27-ha study area, M1 and M2 (named after the drone missions), define the clipped area used in this project. The star on the inset map represents the study area in the context of the northwestern US. True color drone orthomosaic imagery (collected using a MicaSense MX-RedEdge sensor) shown within study areas; basemap imagery outside of drone collection area from USDA National Aerial Inventory Program; basemap in the inset from ESRI. 6

Figure 2.2. Project workflow for evaluating tree-level damage using Structure-from-Motion derived (SfM) point cloud with assigned multispectral reflectances and tree segmentation. Point-level classification includes healthy (green) and damaged (gray and red) classes of each point. Tree segmentation refers to the point cloud segmentation into individual trees. Gray boxes with dashed lines outline the objectives of this project. 9

Figure 2.3. (a) Height-normalization on a subset of the point cloud. Points classified as ground are in light green and non-ground points are in dark green. Visual assessment indicates successful execution of ground classification algorithm (ground-classified points predominantly located at lower elevations) and height normalization operation (flat areas demonstrate the removal of the influence of terrain). (b) Results of the individual tree segmentation (individual trees are represented in different colors). 13

Figure 3.1. Overall accuracy (OA) as a function of the number of variables used in the random forest (RF) models. Points in black are the highest overall accuracies of RF models from the best subsets algorithm of explanatory variable combinations with low multicollinearity. The translucent points with jitter are the rest of the overall accuracies..... 21

Figure 3.2. (a), (b), (c) Examples of trees used to evaluate classification models of healthy versus damaged points. Columns (left to right): true color image, false color image (red-green-near infrared), and results from three random forest models (text indicates explanatory variables in models). Green points correspond to green class, red to red class, gray to gray class, and black to shadow class. Red

and green arrows indicate damaged (gray and red classes) and healthy areas, respectively where the second-ranked three-variable model (RBI + NDVI + REDEGDE model) agrees better with a visual assessment than the other models. 23

Figure 3.3. An example of a top-killed tree with lower classification confidence (reported upon application of the random forest (RF) model) for areas on trees with ambiguous health status based on RF-model and visual inspection (red arrow). (a) True color representation of the point cloud. (b) RF classification; green is the healthy class, red is the red class, gray is the gray class, and black is shadow. (c) The probabilities of classes that are shown in (b); darker colors represent higher probabilities and therefore confidence in the classification. 25

Figure 3.4. Example of branch flagging observed in a tree. (a) True color image. (b) False color image. (c) Random forest model classification; green points are the green class, red is the red class, gray is the gray class, and black is the shadow class. (d) The probability of classes shown in (c); darker colors represent higher probabilities and therefore higher confidence). 29

Figure 3.5. Distributions of classification probabilities of points classified as (a) "*green*" class, (b) "*gray*" class, (c) "*red*" class, and (d) "*shadow*" class. Frequencies were normalized by the maximum number of points per bin in each histogram to allow for comparison among classes. 30

Figure 3.6. Zoomed-in views of tree-level damage metrics for a part of the study site. The basemap imagery is the true color drone orthomosaic (collected using a MicaSense MX-RedEdge sensor). Polygons delineate the crown of individual trees. (a) Damage type identification. (b) Percentage of top-kill relative to tree height for trees identified as "*top-kill*". Trees identified as "*healthy*" or "*non-top-kill*" are not outlined. (c) Average probability of point-level classifications for each tree. 33

Figure 3.7. Tree-level damage metrics for the study area. Polygons cover the crown of each tree. The basemap imagery is the true color drone orthomosaic (collected using a MicaSense MX-RedEdge sensor). (a) Damage type identification. (b) Percentage of top-kill relative to tree height for trees identified as "*top-kill*". Trees identified

as “*healthy*” or “*non-top-kill*” are not outlined. (c) Average probability of classification for all points in each tree. 34

Figure 3.8. Spatially aggregated maps (30-m spatial resolution) produced from tree-level damage maps. (a) Mean percentage of damage (red plus gray) for trees within the grid cell. (b) Modal damage type of trees within the grid cell. (c) Mean top-kill length (m) for top-kill trees within the grid cell. The first class (0.00-0.25) indicates grid cells with predominantly healthy or non-top-kill trees. (d) Mean percentage of top-kill relative to the tree height within the grid cell..... 35

1. Introduction

Forests are integral components of the biosphere that provide ecosystem services such as habitat, nutrient and water cycling, absorption of air pollutants, and carbon sequestration (Anderegg et al., 2020, 2015). From an economic and societal standpoint, the maintenance of forests ensures the sustainable supply of harvested goods (e.g., timber, fuel, and bioproducts), and many communities value forests as spaces for cultural traditions and recreation (Arneth et al., 2019; Pearce, 2001). Forests provide a diverse range of benefits to humans and the ecosystem, hence, monitoring of tree health status is important for the sustainable management of forests.

Insect disturbances account for a large fraction of tree mortality in many forest ecosystems (Hartmann et al., 2022; Hicke et al., 2016; Pureswaran et al., 2018), including forests in the western United States (Cohen et al., 2016). Insect outbreaks have played a vital role in maintaining forest ecosystems, however, the recent rise in average temperatures due to anthropogenic climate change has allowed for faster insect development periods and reduced host fitness from increased drought stress, thereby increasing insect population abundance, range, and winter survival (Anderegg et al., 2015; Pureswaran et al., 2018). Because of these factors, the severity, frequency, and duration of insect outbreaks are projected to amplify in the future, increasing tree mortality in forest ecosystems globally (Anderegg et al., 2020, 2015; Bentz et al., 2010; Hall et al., 2016; Hicke et al., 2022; Pureswaran et al., 2018).

Remote sensing offers a wide range of data available at various spatial and temporal scales and resolutions (Lausch et al., 2016), allowing researchers and management personnel to cater their data collection requirements to the scope of their program objectives. In the case of detection and monitoring of forest disturbances, remote sensing can provide a cost-effective alternative due to its lower cost of data acquisition per unit area compared with traditional labor-intensive field data collection over large spatial extents (Hall et al., 2016; Rhodes et al., 2022). As such, remote sensing can be useful for the monitoring of insect outbreaks over large areas at fine resolutions as tree damage and mortality are often sparse (Senf et al., 2017).

Forest insect outbreaks can be detected through the remote sensing of characteristic traits associated with tree damage and mortality caused by insects (e.g., spectral or thermal signatures) (Lausch et al., 2016; Luo et al., 2023). The USDA Forest Service (USFS) identifies these visible traits in their aerial detection surveys (ADS) using the following damage classes to assess the extent and severity of forest insect outbreaks: mortality, discoloration, dieback, branch flagging, branch breakage, mainstem broken or uprooted, defoliation, and top-kill (Ciesla et al., 2015). Classes such as these can be used to attribute damage to specific biotic damage agent and stage of infestation. For example, top-kill is defined as the death of branches of the upper parts of the crown (Ciesla et al., 2015; Wickman, 1979). Top-kill occurs in the early infestation stages of Douglas-fir tussock moth (DFTM) (*Orgyia pseudotsugata*) (Pederson et al., 2020), western spruce budworm (WSBW) (*Choristoneura freemani*) (Ciesla et al., 2015; Fellin and Dewey, 1986), and fir engraver (*Scolytus ventralis*) (Ferrell, 1986) and is an indicator of the severity of defoliation (Hall et al., 2006, 1998).

In recent years, the availability of reasonably priced uncrewed aerial systems (UAS, herein referred to as “drones”) has led to an increase in forest ecology studies using drone-based sensors and photogrammetry techniques (Dainelli et al., 2021; Rhodes et al., 2022). The detection and monitoring of insect infestations is a prominent area of focus for drone-based forest remote sensing research, as predicted by Hall et al. (2016) and Senf et al. (2017). In their review of studies monitoring forest health with drone-based remote sensing, Ecke et al. (2022) stated that a majority of studies focused on the remote sensing of insect outbreaks.

Products from drone-based remote sensing and photogrammetry can be broadly categorized into two groups: point cloud (three-dimensional (3D)) data and imagery (two-dimensional (2D)) data. Point cloud data provide the structural representation of objects such as trees (Aber, 2019) and are useful in providing insight into the variability and structure of forest ecosystems and disturbances (Duarte et al., 2022; Ecke et al., 2022; Guimarães et al., 2020). Drone-based remote sensing with active sensors such as light detection and ranging (LiDAR) provide point clouds (Guimarães et al., 2020), yet can be relatively expensive compared to the more common passive sensors such as multispectral and Red-Green-Blue (RGB) sensors (Duarte et al., 2022). Data from these passive sensors are stored as imagery containing 2D

attributes (Jensen, 2016). In addition to their use as images, advances in computer vision and image processing algorithms such as Structure-from-Motion (SfM) (Westoby et al., 2012) have made it possible to use overlapping images captured by drones to create 3D reconstructions of the features present in the remotely sensed scene (Aber, 2019; Guimarães et al., 2020; Westoby et al., 2012).

Common data products generated from point clouds are the digital surface model (DSM; elevations of features), digital terrain model (DTM; elevations of bare ground), canopy height model (CHM), and stitched orthomosaic (Aber, 2019). The DSM and DTM are 2D images generated from the ground and non-ground classification of the point cloud (Aber, 2019; Mohan et al., 2021). The CHM is a 2D image representing the height of features in the scene derived from the DSM and DTM (Aber, 2019; Mohan et al., 2021). Two-dimensional orthomosaic images that contain attributes such as reflectances are generated using the DSM and the individual images taken by the drone (Aber, 2019).

The point cloud and the 2D images containing height information (i.e., DSM, DTM, CHM) are often used for extracting structural properties of remotely sensed objects such as position and height (Guimarães et al., 2020). In drone-based remote sensing studies of forests, the height information is commonly used for individual tree detection and crown delineation (herein referred to as "tree segmentation") (Duarte et al., 2022; Ecke et al., 2022; Guimarães et al., 2020). In most studies of tree health to date, the 3D data are only used in an intermediary step (i.e., for tree segmentation) (Duarte et al., 2022; Guimarães et al., 2020).

Most drone studies assessing tree health in forests use the 2D orthomosaic of multispectral data for visual assessment of the study site and for extraction of the spectral properties of features (e.g., trees) present in the remotely sensed scene (Ecke et al., 2022; Guimarães et al., 2020). Some studies have used both spectral and structural information to produce 2D products assessing tree health (Ecke et al., 2022). Cardil et al. (2019) used SfM-derived point cloud data for tree segmentation but used only spectral information to classify pine processionary moth (*Thaumetopoea pityocampa*)-caused defoliation levels of trees using vegetation indices with good overall accuracy (OA; 82-87%). Abdollahnejad and Panagiotidis (2020) used height information from the CHM derived from a point cloud for texture analysis, subsequently combining the information from the texture analysis with

spectral information in a support vector machine model to classify tree species and tree health status. The combination of structural information provided by texture analysis and spectral information was only useful for improving tree species classification but not for tree health status classification (Abdollahnejad and Panagiotidis, 2020). Cessna et al. (2021) extracted structural metrics from a SfM point cloud (such as height and 3D grouping of points) and spectral information from the multispectral orthomosaic in a study of spruce beetles. Trees were identified using on-screen manual digitization, and the authors developed models that mapped tree health (Cessna et al., 2021). The authors found that models that used only structural information had higher accuracy compared (OA: 75-77%) with models that used only spectral information (OA: 55-62%) and adding spectral information to structural information did not increase the accuracy significantly (Cessna et al., 2021).

Given the extent of forest insect outbreaks and their probable increase in the future due to climate change, there is a need for advancing mapping methods that address not only tree mortality but also other types of damage, such as top-kill and branch flagging (dead or discolored branches (Ciesla et al., 2015)). Such methods will help with tree health monitoring and aiding in the attribution of damage to different biotic agents, including bark beetles and defoliators. Despite the increasing use of drones in studies of insect outbreaks, no studies have combined the resulting data products (i.e., multispectral and point cloud data) for analysis in a 3D environment.

To address the above research need, I examined the utility of combining 3D structure data with multispectral data to detect damage on parts of individual conifer trees in a forested area in western Montana damaged by insects. I developed a novel approach to detect tree damage using multispectral information within the 3D point cloud. I then calculated the amount of damage for each tree and analyzed the vertical location of damage to identify the presence and estimate the length of top-kill. This project had the following objectives:

I. Segment individual trees within the study area using the SfM point cloud.
II. Develop, evaluate, and apply a classification of points into healthy (green) or damaged (gray and red) based on their multispectral reflectances.
III. Develop, evaluate, and apply an algorithm for identifying percent damage, damage type, and top-kill metrics of individual trees.

2. Methods

2.1 Study area

The study area was part of a broader project assessing tree damage using remote sensing. Site selection was based on inspection of tree damage caused by defoliators and bark beetles from USFS ADS and existing satellite imagery. An area that experienced outbreaks of defoliators and bark beetles over the last 15 years was identified on Sheep Mountain east of Missoula, Montana (46°57'34.3" N, 113°46'17.1" W) (Figure 2.1, Appendix A). The defoliators included western spruce budworm (WSBW) and Douglas-fir tussock moth (DFTM), and the bark beetles included mountain pine beetle (*Dendroctonus ponderosae*) and Douglas-fir beetle (*Dendroctonus pseudotsugae*). The study area is at an elevation of around 1676 meters with an annual average temperature of 7°C, and annual average precipitation of 358.4 mm (NOAA, 2021). Common tree species are subalpine fir (*Abies lasiocarpa*), lodgepole pine (*Pinus contorta*), and Douglas-fir (*Pseudotsuga menziesii*).

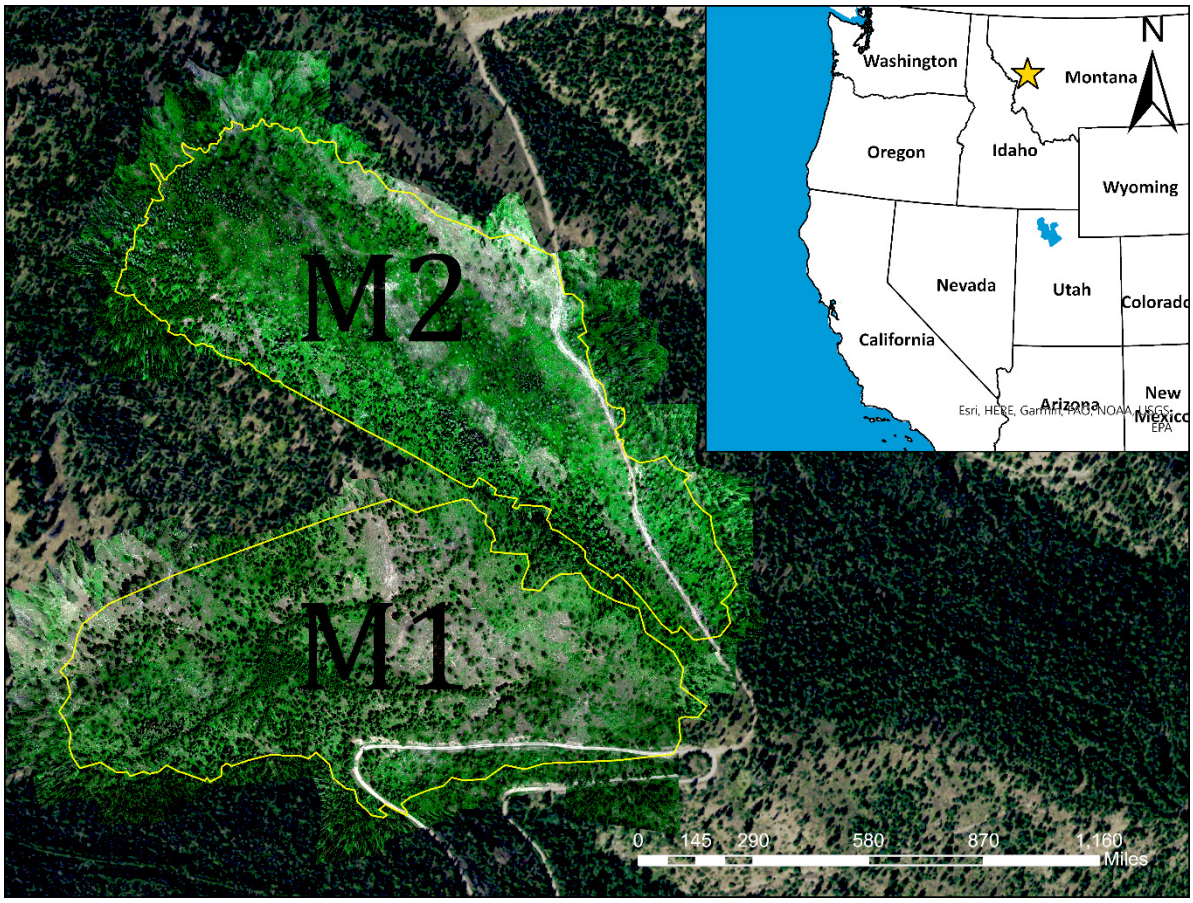

Figure 2.1. Yellow polygons around the 27-ha study area, M1 and M2 (named after the drone missions), define the clipped area used in this project. The star on the inset map represents the study area in the context of the northwestern US. True color drone orthomosaic imagery (collected using a MicaSense MX-RedEdge sensor) shown within study areas; basemap imagery outside of drone collection area from USDA National Aerial Inventory Program; basemap in the inset from ESRI.

2.2 Drone imagery collection

Drone imagery was collected in two missions on June 27, 2022, around 12 pm (M1) and 1:30 pm (M2) over a study area of 27-ha (Figure 2.1). A DJI Matrice-210 drone with a MicaSense MX-RedEdge sensor (herein referred to as "MS sensor") and Zenmuse XT2 RGB sensor (herein referred to as "RGB sensor") was used for image acquisition. The MS sensor unit is a radiometrically calibrated 5-band sensor capable of collecting data in the blue (475±10 nm; center wavelength and bandwidth), green (560±10 nm), red (668±5 nm), red edge (717±5 nm), and near-infrared (840±20 nm) wavelengths (MicaSense, Inc, 2023). The sensor has five 1.2 megapixel imagers (one per band), which have a ground sampling distance of 8 cm at a flight altitude of 120 m (MicaSense, Inc, 2023). The RGB sensor collects data in the visible wavelengths of the electromagnetic spectrum; the instrument is not radiometrically calibrated.

Mission flights consisted of a single-grid flight path with 80% frontal overlap and 75% side overlap for each image with an average flight altitude of 91 meters above the ground (Appendix A). The flight parameters were established with the objective of simultaneous image acquisition from all three sensors. Fourteen ground control point (GCP) markers were placed across the drone mission areas to aid in orthorectification; GPS points were logged for each GCP with a Trimble Geo X7 GPS receiver.

2.3 Drone imagery pre-processing

The images collected from the RGB and MS sensors were used to generate two dense point clouds and two orthomosaics (one set from each sensor) in Agisoft Metashape Professional (v1.8.4 build 14671; herein referred to as "Metashape") using SfM photogrammetry. The point cloud and orthomosaic from the RGB sensor and the orthomosaic from the MS sensor were used to identify reference points and trees and for qualitative inspection of results (i.e., as guides). The point cloud from the MS sensor was used in the classification and subsequent analysis of tree damage.

The SfM approach in Metashape creates an estimated 3D model that represents the orientation and location of individual cameras in a 3D space (Agisoft Metashape, 2023;

Westoby et al., 2012). SfM reconstruction of the (initial) estimated 3D model of the study area is dependent on the detection and matching of unique points (tie-points) occurring in overlapping images (Aber, 2019). This estimated 3D model is created using the image alignment workflow in Metashape, which allows the user to set the accuracy of the 3D model construction (Agisoft Metashape, 2023). The accuracy parameter was set to "*high*" based on the findings of studies of optimal parameter settings for tree detection and segmentation (Tinkham and Swayze, 2021; Young et al., 2022).

The estimated 3D models from the RGB and MS sensors (one model from each sensor) were optimized with post-processed GCPs with visual assessment and manual adjustment of marker positions identified by Metashape (where necessary) for at least 15 images per GCP. The estimated 3D models were reoptimized in Metashape with adaptive model fitting and tie point covariance estimations based on the GPS data of the manually assessed GCP markers. Low-quality tie points with high reconstruction uncertainty and high reprojection errors were identified and removed using the "*gradual selection*" tool in Metashape, and the estimated 3D models were reoptimized (James et al., 2017). The (final) dense point clouds were generated from the estimated 3D models. Processing reports were generated from Metashape before and after model optimization to report the improvement in positional errors (root mean square error, RMSE).

The final point cloud generated from the RGB sensor was used to produce an orthomosaic at ~2 cm spatial resolution (herein referred to as "RGB orthomosaic"), and the final point cloud from the MS sensor was used to produce the "MS orthomosaic" from the radiometrically calibrated multispectral images (~6 cm spatial resolution) (Figure 2.2). Multispectral values from the images were assigned to the final point cloud from the MS sensor (Appendix B.2; herein referred to as "point cloud").

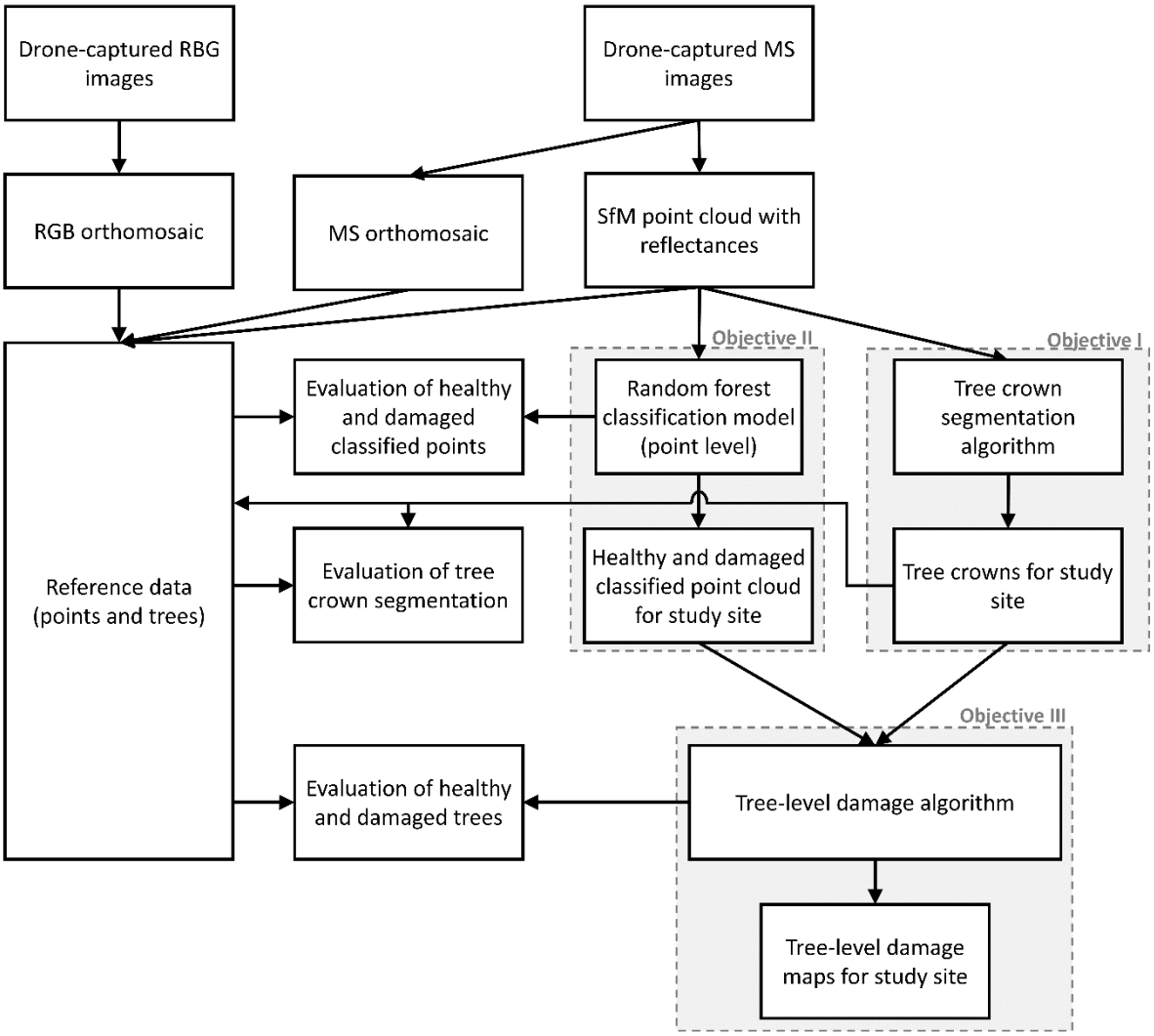

Figure 2.2. Project workflow for evaluating tree-level damage using Structure-from-Motion derived (SfM) point cloud with assigned multispectral reflectances and tree segmentation. Point-level classification includes healthy (green) and damaged (gray and red) classes of each point. Tree segmentation refers to the point cloud segmentation into individual trees. Gray boxes with dashed lines outline the objectives of this project.

2.4 Reference data

Following the approaches of multiple studies (e.g. Cardil et al., 2019; Cessna et al., 2021; Otsu et al., 2019, 2018; Zhang et al., 2020), the RGB and MS orthomosaics were used for assembling the reference data sets used in the training and evaluation of a) tree segmentation, b) the classification of individual points by health status, and c) the identification of trees into healthy or damaged (Figure 2.2). I used the MS orthomosaic as the primary reference imagery and used the finer-resolution RGB orthomosaic as well as individual MS and RGB drone images to provide additional information.

I generated a random set of 1000 point locations across the study site for on-screen identification of trees ("*tree*" class), and understory vegetation and ground ("*not tree*" class) and used this data set for evaluating tree segmentation.

For training the classification of individual points and the algorithm to label tree damage, I identified a set of 100 trees across the study area consisting of healthy trees, non-top-kill and top-kill trees with minor damage, moderate damage, major damage, and dead trees (Appendix C) using on-screen delineation of tree crowns with the MS and RGB orthomosaics. Additionally, I generated a random set of 1000 trees and identified the damage type of each tree on-screen; this set of trees was used for evaluating the tree-level damage algorithm (independent of the 100 trees used for training).

For training and testing the point classification, I identified 800 points that represented the health status of parts of trees (points in the point cloud), including healthy (green) and damaged (gray and red) classes (Appendix C). These points were located on the reference data set of trees described above.

2.5 Tree segmentation

2.5.1 Ground and non-ground classification, and height-normalization of point cloud

I used a progressive morphological filter algorithm developed by Zhang et al. (2003) to classify ground and non-ground points using the "*classify_ground*" function available in the "*lidR*" package (Roussel et al., 2022). The progressive morphological filter algorithm requires two parameters, a sequence of window size values (set to 0.75, 3, and 0.75 m) and a height threshold value (set to 2m) (Figure 2.3a).

I used the "*normalize_height*" function from the "*lidR*" package (Roussel et al., 2022) to generate a height-normalized point cloud from the ground and non-ground classified point cloud, thereby removing the influence of terrain (Mohan et al., 2021) (Figure 2.3a). The "*algorithm*" parameter was set to K-nearest neighbor with an inverse distance weighting algorithm using the "*knnidw*" function (Roussel et al., 2022).

2.5.2 Point cloud segmentation into unique tree objects

Common tools for segmenting individual trees in drone-based RS of forests are image-based algorithms that use the CHM and point cloud-based algorithms that operate on an individual point level (Guimarães et al., 2020) (Appendix D). I conducted a case study with a subset data of the study area to compare an image-based algorithm by Silva et al. (2016) with a point cloud-based algorithm by Li et al. (2012) (Figure D1). Based on the case study, the point cloud-based segmentation algorithm by Li et al. (Li et al., 2012) was applied to the point cloud of the study area using the "*segment_trees"* function with the "*li2012*" algorithm from the "*lidR*" package (Li et al., 2012; Roussel et al., 2022) (Figure 2.3b).

I used the "*crown_metrics*" function from the "*lidR*" package (Roussel et al., 2022) with the point cloud with tree segmentation as input which resulted in a polygon feature layer of tree crowns. I performed an accuracy assessment of the tree segmentation using the reference data set of 1000 randomly generated point locations identified as "*tree*" and "*not tree*" (described above), producing a confusion matrix, and computed the omission and commission errors of each class and overall accuracy.

A second accuracy assessment of the tree segmentation was performed using the reference dataset of 100 trees consisting of manually delineated tree crowns. This accuracy assessment compared areas of tree crowns from the tree segmentation algorithm and manually delineated tree crowns (reference data set) using Sørensen's coefficient (SC) (Cardil et al., 2019; Legendre et al., 1998). SC is defined as:

$$SC = \frac{(2 * A)}{(2 * A) + B + C}$$

(Equation 1)

A is the area identified as tree crown from both the manual delineation and the tree segmentation, *B* is the tree crown area from the tree segmentation algorithm but not the manual delineation, and *C* is the tree crown area from the manual delineation but not the tree segmentation algorithm (Figure D3) (Cardil et al., 2019). The SC value ranges from 0 to 1, where values close to 0 indicate lower agreement and values close to 1 indicate higher agreement (Cardil et al., 2019; Legendre et al., 1998).

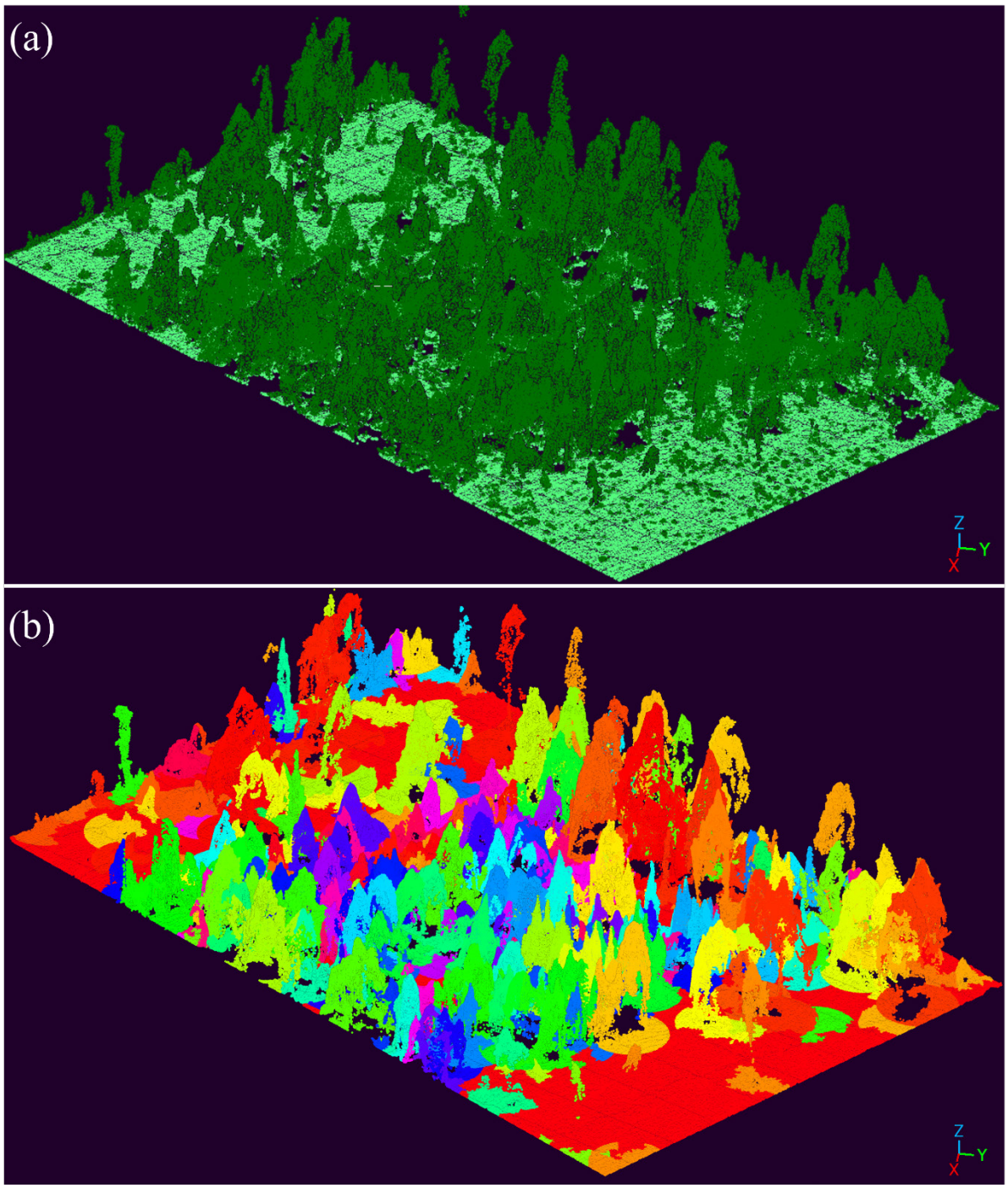

Figure 2.3. (a) Height-normalization on a subset of the point cloud. Points classified as ground are in light green and non-ground points are in dark green. Visual assessment indicates successful execution of ground classification algorithm (ground-classified points predominantly located at lower elevations) and height normalization operation (flat areas demonstrate the removal of the influence of terrain). (b) Results of the individual tree segmentation (individual trees are represented in different colors).

2.6 Point-level classification with random forest models

I developed models for classifying the point cloud into green, gray, red, and shadow class points that represent the health status of areas on trees that are healthy (green) and damaged (gray and red) using the spectral values and indices of the reference data set of points in the point cloud (Figure C1).Vegetation indices (Table 2.1) were calculated for each point of the reference data set.

Table 2.1. Name, equation, and reference for vegetation indices used in the project. ρ is reflectance.

Name (abbreviation)	Equation	Reference
Red-Green Index (RGI)	ρ_{red}/ρ_{green}	Gamon and Surfus (1999)
Simple ratio (SR)	ρ_{NIR}/ρ_{red}	Woebbecke et al. (1995)
Normalized Difference Vegetation Index (NDVI)	$(\rho_{NIR} - \rho_{red})/(\rho_{NIR} + \rho_{red})$	Rouse et al. (1974)
Normalized Difference Red Edge (NDRE) Index	$(\rho_{NIR} - \rho_{rededge})/(\rho_{NIR} + \rho_{rededge})$	Hunt Jr. et al. (2011)
Green Leaf Index (GLI)	$\frac{\left((\rho_{green} - \rho_{red}) + (\rho_{green} - \rho_{blue})\right)}{\left((2 * \rho_{green}) + \rho_{red} + \rho_{blue}\right)}$	Hunt Jr. et al. (2011)
Excess Green (ExG) Index	$(2 * \rho_{green}) - \rho_{red} - \rho_{blue}$	Woebbecke et al. (1995)
Red-Blue Index (RBI)	ρ_{red}/ρ_{blue}	Perez et al. (2018)
Mean Red-Green-Blue (meanRGB) Index	$(\rho_{red} + \rho_{green} + \rho_{blue})/3$	Clay et al. (1997)

Random forest (RF) classification is the most commonly used modeling tool in drone-based studies of forest insects (Duarte et al., 2022; Guimarães et al., 2020). RF models are nonparametric and nonlinear machine learning models with the ability to handle complex data with multiple predictor variables and higher dimensions (Breiman, 2001; Qi, 2012).

An objective was to provide insights about important spectral regions useful for damage detection, thereby enabling the application of similar methods in different situations (Stahl et al., 2023). One relevant issue is multicollinearity, which can occur when evaluating explanatory variables (Graham, 2003). High degrees of correlation are common in remote sensing data with spectral indices (). From the set of 13 potential predictor variables (five spectral bands and eight spectral indices), a subset of predictor variables with low multicollinearity was selected (Figure E1). I used a "best subsets" approach for selecting the predictor variables in the final model.

In this study, the best subsets approach is an iterative method that creates RF models from combinations of potential predictor variables. RF models were generated using the "*randomForest*" package with 500 trees per model (Liaw and Wiener, 2002). RF models classified each of the 800 points of the reference data set (described above) into green, gray, red, and shadow classes representing tree health status of healthy (green) and damaged (gray and red) areas on trees. Models were ranked based on overall accuracy (OA). To avoid multicollinearity effects, models were only considered if the maximum pairwise absolute correlation coefficient between predictor variables was less than 0.7. Predictor variable subsets of one variable, two variables, up to four variables were considered. No five-variable subset had a maximum pairwise correlation of less than 0.7.

A set of the most accurate RF models was applied to a subset of the study site for further evaluation using the reference data set of trees (described above). I visually compared classified points on reference trees to the individual MS and RGB images. The RF model with high OA and the best ability to capture the tree health condition was selected as the final RF model and applied to the point cloud of the study area.

2.7 Tree-level damage algorithm

I developed an algorithm to separate trees into healthy versus different damage types. This algorithm used the results of the tree segmentation and the point-level RF classification of healthy and damaged points as input (points classified as ground and shadows were not included).

The algorithm followed a three-step procedure. The first step involved calculating the percentage of green, gray, red, and damaged points (sum of gray and red points) for each tree. Trees with less than five percent damage were identified as "*healthy*" trees, and the remaining trees were identified as "*damaged*" trees.

I used the set of 1000 trees from the reference data (described above) to perform an accuracy assessment of the separation of healthy versus damaged trees. The algorithm was evaluated with a sampling (with replacement) of 200 trees per class (i.e., "*healthy*" and "*damage*" classes). The sampling was repeated 500 times and average values were reported in the final confusion matrix.

In the second step, the "*damaged*" trees were separated into the following damage types: "*minor damage*" (5-25% damaged (red plus gray) points), "*moderate damage*" (25-75% damaged points), "*major damage*" (75-90% damaged points), and "*dead*" (>90% damaged points). The trees identified as "*dead*" were separated into "*dead (red)*" (>75% red points), "*dead (gray)*" (>75% gray points), and "*dead (mixed)*" (remainder of "*dead*" trees) (Figure H1).

To evaluate the separation of healthy and the different damage types, the balance among the number of trees per class was improved by sampling (with replacement) of "*healthy*" (n = 75) and "*minor damage*" (n = 25) classes. The sampling was repeated 500 times and average values were reported in the final confusion matrix.

In the third step, "*damaged*" trees were assessed for top-kill and identified as "*non-top-kill*" or "*top-kill*" using one of two algorithms described below. Top-kill trees are those that have continuous and nearly complete damage starting from the top of the tree extending downward (Wickman, 1979). For "*top-kill*" trees, I estimated the top-kill height (defined as

the distance between the ground and the lowest top-kill bin), the length of top-kill (defined as the distance in meters from the top of the tree to the bottom of top-kill) and the percentage of top-kill (top-kill length relative to total tree height).

Visual inspection of trees indicated variability in the crown characteristics of top-killed trees, and therefore two top-kill algorithms were developed: the "*top2bin*" algorithm analyzes cumulative damage from the treetop to the incremental bin, and the "*bin2bin*" algorithm analyzes damage one bin at a time (Figure H2). The two top-kill algorithms use an iterative approach of evaluating damage at height intervals (bins) of 0.25 m starting at the treetop and progressing downward by bin.

The "*top2bin*" algorithm considers the percentage of all damaged (red plus gray) points from the top of the tree to a given height bin, stopping when the percentage is <80%. The "*bin2bin*" algorithm assesses the percentage of damaged points within each height bin, stopping when the percentage within is <90%. If the algorithms stop at the topmost bin, the tree is identified as "*non-top-kill*". A sensitivity test revealed little difference between top-kill estimated with an 80% damage threshold using the "*top2bin*" algorithm and top-kill estimated with a 90% damage threshold using the "*bin2bin*" algorithm (Figure H3). Hence, the "*bin2bin*" algorithm used a 90% damage threshold (within a bin) to maintain a strict (and better) estimation of top-kill on "*minor damage*" and "*moderate damage*" trees and the "*top2bin*" algorithm used an 80% damage threshold (across bins from the top-down) for accurate estimation of top-kill on "*major damage*" and "*dead*" trees.

The choice of implementation between the two algorithms is based on the percentage of damage points on a tree. An assessment of reference trees with top-kill revealed that the stricter and more conservative "*bin2bin*" algorithm provided better top-kill estimates for all "*minor damage*" and most "*moderate damage*" trees, whereas the more lenient "*top2bin*" algorithm provided better top-kill estimates for all "major damaged" and "dead" trees. Hence, the "*top2bin*" algorithm was used for trees with greater than 50% damaged points (of the total points for a tree), and the "*bin2bin*" algorithm was used for the remaining trees.

The subset of "*damaged*" identified trees from the reference data set of 1000 trees was used to evaluate the performance of the algorithm that identifies "*non-top-kill*" and "*top-kill*" trees. The balance among the number of trees per class was improved by sampling (with

replacement) of "top-kill" class (n = 40). The sampling was repeated 100 times and average values were reported in the final confusion matrix.

2.8 Characterization of the extent of tree damage across the UAV scene

I applied the final RF model to the point cloud resulting in green, gray, red, and shadow classified points. Additionally, the class probability returned by the final RF model, useful for assessing the confidence of RF classification for each point, was included in the point cloud, and class probabilities were then averaged for each tree. The RF model computes class probabilities for each point based on the average proportion of votes for each class across all the trees (Breiman, 2001). For example, if a point is classified as "*green*" by 439 out of 500 trees, the point will be classified as "*green*" class with a probability of (439/500 = 0.88). The estimated probabilities generated from Random Forest (RF) models, that provide insights and interpretations into classification confidences, are unrestricted by assumptions about the dataset (e.g., distribution) – often required for regression-based models (Malley et al., 2012).

I applied the tree-level damage algorithm using the tree segmentation results and the classified point cloud to compute damage type and metrics for each tree. Damage metrics included the percent green, percent gray, percent red, and percent damage (gray plus red) for each tree. The length of top-kill and percent top-kill were calculated for each top-kill tree.

Spatially aggregated maps derived from tree-level data are useful for understanding and management. I spatially aggregated the tree-level damage type and metrics into 30 x 30-meter resolution rasters. Tree crowns were converted to centroids, and the modal damage type and mean damage metrics of trees (centroids) falling within a grid cell were computed.

3. Results

The drone imagery acquisition over the 27-ha study area resulted in set of 8800 images from the calibrated MicaSense multispectral sensor (one capture from the sensor stores five images, one per band; 1760 total captures) and 839 images from the uncalibrated Zenmuse RGB sensor. On a workstation with an Intel Xeon processor with 8 cores running at 3.5 Ghz and 32 Gb RAM, pre-processing of the drone imagery took ~2.5 hours to produce the point clouds for the study site. Processing time for the tree segmentation was 6 hours, the application of point classification model took 20 minutes, and execution of the tree damage algorithm took 3 minutes. The sparse point cloud optimization and GCP marker corrections reduced the average positional errors in X, Y, and Z from 1.85 m, 0.89 m, and 1.12 m to 0.02 m, 0.06 m, and 0.05 m respectively, and reduced the total mean positional error from 2.43 m to 0.08 m (Table B1).

3.1 Tree segmentation

The evaluation of the tree segmentation (Li et al., 2012) resulted in an overall accuracy of 61.3% (Table 3.1). The commission error for the "*tree*" class was 12.4% and the omission error was 58.7%. The commission error for the "*not tree"* class, which included cases when the algorithm detected a tree segment, but no co-located reference tree was identified, was 49.1% and the omission error was 8.8%.

All of the 352 cases of the reference trees misclassified as the "*not tree*" class were caused by the algorithm dividing a single tree into multiple trees (over-segmentation) combined with the reference point (identified as a tree) falling in between these over-segmented tree crown polygons (Figure D2). Of the 35 cases of the "*not tree*" reference points misclassified as the "*tree*" class, 31 were due to over-segmentation and the reference point identified as on the ground or understory vegetation but falling within the erroneously delineated tree crown (Figure D2). Four cases were misclassification of ground patches as trees.

The second accuracy assessment comparing manually delineated and tree segmentation crown areas resulted an SC of 0.79, which indicated high agreement.

Table 3.1. Confusion matrix and accuracy metrics of the accuracy assessment of the point cloud-based tree segmentation algorithm (Li et al., 2012). "*Tree segmentation issue*" refers to either the reference point (identified as a tree) falling in between crown segments of a single tree that were divided into multiple trees (over-segmentation) or the reference point (identified as on the ground or understory vegetation) falling within the erroneously delineated tree crown. "*Ground issue*" refers to the misclassification of understory or ground as trees.

		Reference				
	Class	Tree	Not tree	Total	Commission error (%)	User accuracy (%)
Prediction	Tree	248	35 (31: tree segmentation issue; 4: ground issue)	283	12.4	87.6
	Not tree	352 (352: tree segmentation issue)	365	717	49.1	50.9
	Total	600	400	1000		
	Omission error (%)	58.7	8.8		**Overall accuracy**	61.3%
	Producer accuracy (%)	41.3	91.2			

3.2 Point-level classification into health status classes

The overall accuracy of the top classification models of the health status of points increased from one- to four-variable models (Figure 3.1). A substantial increase in accuracy occurred from one- to two-variable models, a minor increase occurred from two- to three-variable models, no increase occurred from three- to four-variable models, and the variation (spread) of overall accuracies decreased with the increase in explanatory variables for RF models with more than one predictor variable (Figure 3.1). Therefore, only the two- and three-variable models were considered further.

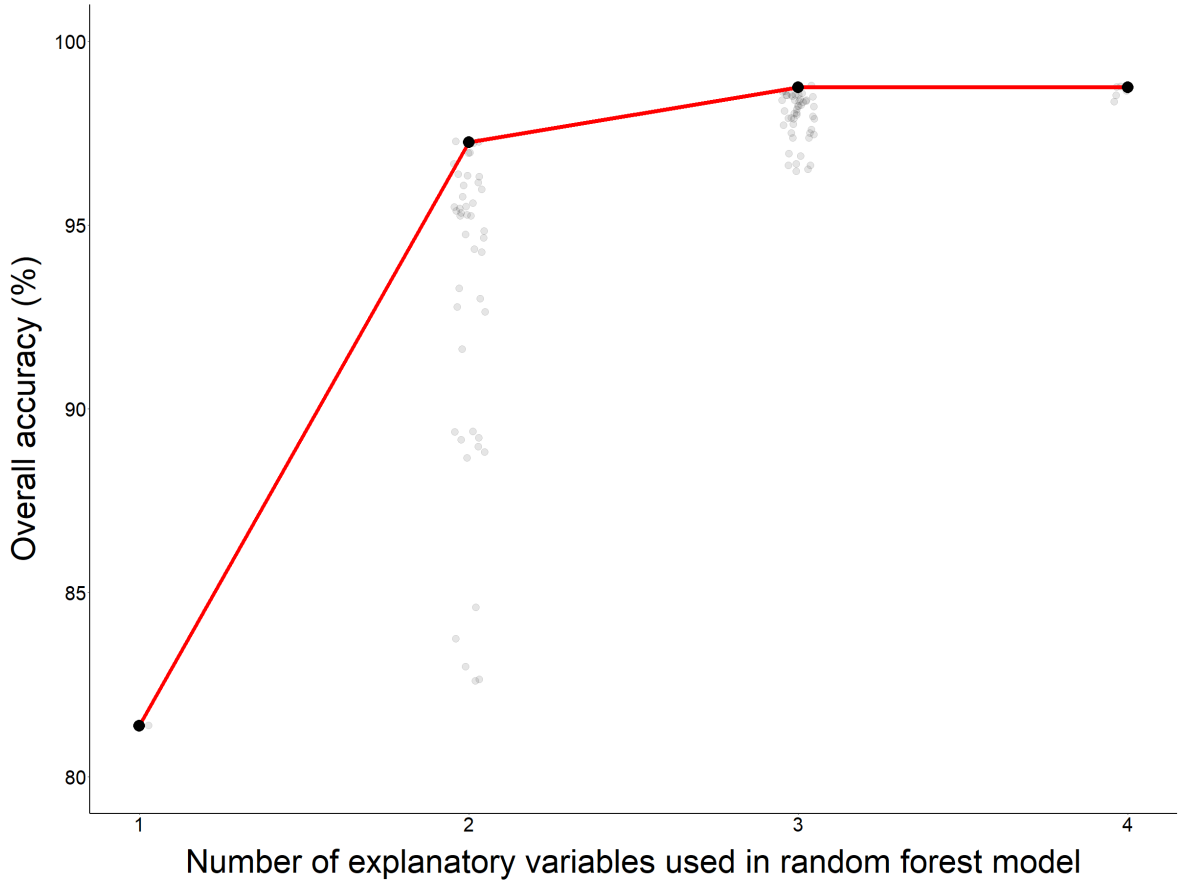

Figure 3.1. Overall accuracy (OA) as a function of the number of variables used in the random forest (RF) models. Points in black are the highest overall accuracies of RF models from the best subsets algorithm of explanatory variable combinations with low multicollinearity. The translucent points with jitter are the rest of the overall accuracies.

The top five two-variable models had very similar results in terms of overall accuracy (Table F1). Therefore, only the top-ranked model two-variable model was used for comparison with

the top three-variable models. Indices computed using RGB only bands, such as RGI, RBI, meanRGB, and GLI were common amongst the top performing two-variable and three-variable models and the most common spectral band was the green band (GRE) (Table F1).

The top-ranked model two-variable model and the top five three-variable models were similar in terms of overall accuracy (Table F1). Case studies of several reference trees were evaluated to further assess differences among models (Figure 3.2). The classification of points by the second-ranked three-variable model (RBI + NDVI + REDEDGE model) best represented damage locations of the reference trees (Figure 3.2). This model had an overall accuracy of 98.6% and out-of-bag error rate of 1.4% and class error rates of 0-3.5%, very similar to the top-ranked three-variable models (Table 3.2, Table F1). Given the high accuracy and best performance in the visual inspection, the RBI + NDVI + REDEDGE model was selected as the final model and used subsequently. Points with reflectances that were more ambiguous in terms of health status had reduced classification confidence reported by the random forest model (Figure 3.3), although the analysis of case studies and selection of the final model minimized these potential errors.

Some sensors used on drones and satellites do not have red edge or near-infrared bands. Models with predictor variables derived from only visible bands had high accuracy (>97% for two-variable models and > 98.5% for three-variable models). In addition, inspection of reference trees (Figure 3.2) indicated that the RBI + GRE + GLI model captured damaged locations well.

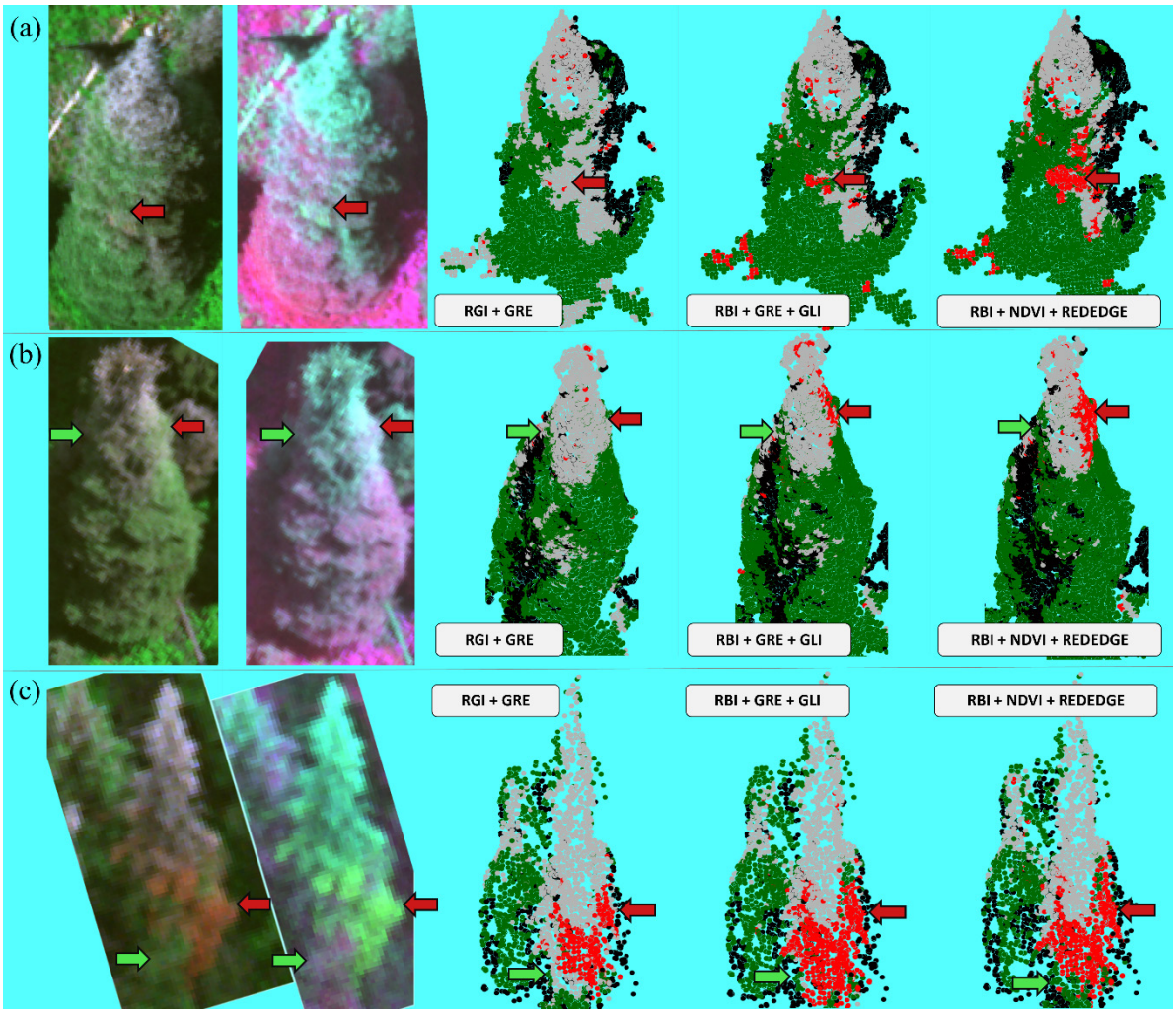

Figure 3.2. (a), (b), (c) Examples of trees used to evaluate classification models of healthy versus damaged points. Columns (left to right): true color image, false color image (red-green-near infrared), and results from three random forest models (text indicates explanatory variables in models). Green points correspond to green class, red to red class, gray to gray class, and black to shadow class. Red and green arrows indicate damaged (gray and red classes) and healthy areas, respectively where the second-ranked three-variable model (RBI + NDVI + REDEGDE model) agrees better with a visual assessment than the other models.

Table 3.2. Confusion matrix and accuracy metrics of the final random forest model (RBI + NDVI + REDEDGE) for classifying points into healthy, damaged, and other classes.

		Reference						
	Class	Green	Gray	Red	Shadow	Total	Commission error (%)	User accuracy (%)
Prediction	Green	199	1	2	2	204	2.0	98.0
	Gray	0	199	5	0	204	2.0	98.0
	Red	1	0	193	0	194	1.0	99.0
	Shadow	0	0	0	198	198	0	100
	Total	200	200	200	200	800		
	Omission error (%)	0.5	0.5	3.5	1.0	**Overall accuracy**: 98.6%		
	Producer accuracy (%)	99.5	99.5	96.5	99.0	Out-of-bag error rate: 1.4%		

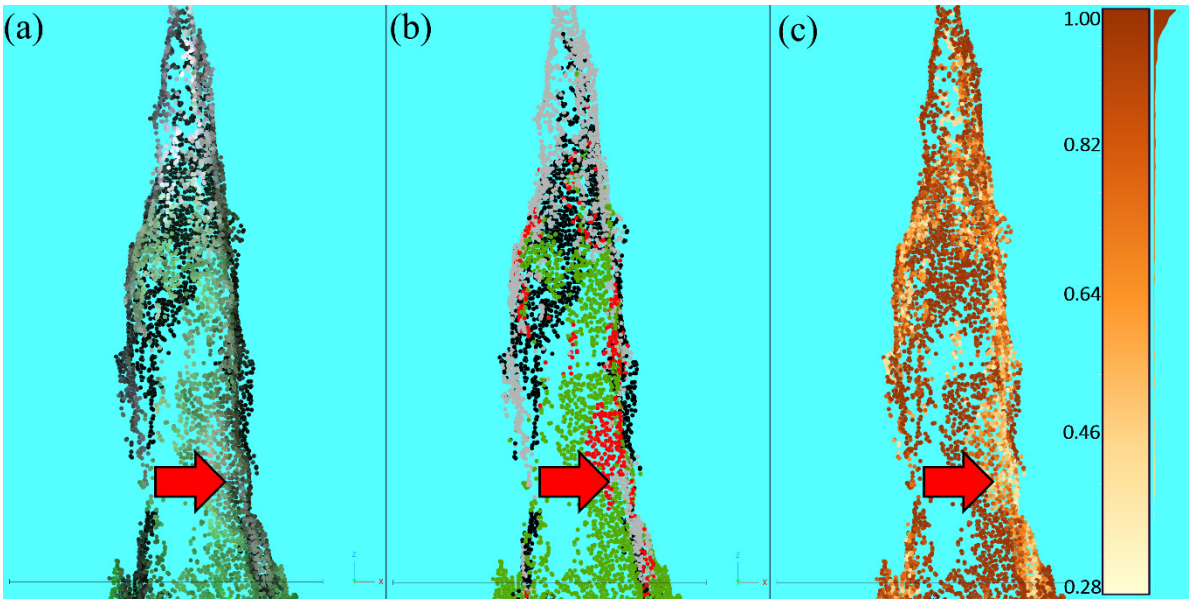

Figure 3.3. An example of a top-killed tree with lower classification confidence (reported upon application of the random forest (RF) model) for areas on trees with ambiguous health status based on RF-model and visual inspection (red arrow). (a) True color representation of the point cloud. (b) RF classification; green is the healthy class, red is the red class, gray is the gray class, and black is shadow. (c) The probabilities of classes that are shown in (b); darker colors represent higher probabilities and therefore confidence in the classification.

3.3 Tree-level damage

The results of the algorithm to separate "*healthy*" and "*damaged*" trees had an overall accuracy of 93.5% (Table 3.3). Omission and commission errors of the classes ranged from 2-11%. The results of the algorithm to separate healthy trees and different types of tree damage had an overall accuracy of 70.2% (Table 3.4), with class omission and commission errors ranging from 0-100%. The greatest confusion was between the "*Dead*" classes ("*red*", "*gray*", "*mixed*") and the "*Major*" and "*Moderate*" damage types, which resulted in high omission and commission errors for all the "*Dead*" sub-classes. High omission errors of 60-100% were likely caused due to errors occurred during the SfM point cloud construction of trees lacking foliage (as discussed below in Discussion)

The results of the algorithm to separate the trees identified as "*damaged*" trees into "*top-kill*" and "*non-top-kill*" had an overall accuracy of 91.8% (Table 3.5 Omission and commission errors of the classes ranged from 5-14%.

Although not a focus of this study, the methods developed here might be used to identify branch flagging on individual trees. An example is shown in Figure 3.4 in which only a portion of the tree's crown was gray (in this case; red parts of a crown might also be detectable).

Table 3.3. Confusion matrix and accuracy metrics for evaluation of algorithm to separate healthy trees from damaged trees. Results are averages from resampling (with replacement; 500 times) to address class imbalance.

		Reference				
	Tree condition	Healthy	Damaged	Total	Commission error (%)	User accuracy (%)
Prediction	Healthy	196	22	218	10.1	89.9
	Damaged	4	178	182	2.2	97.8
	Total	200	200	400		
	Omission error (%)	2.0	11.0		**Overall accuracy**	93.5%
	Producer accuracy (%)	98.0	89.0			

Table 3.4. Confusion matrix and accuracy metrics for evaluation of algorithm to separate healthy trees and different types of tree damage. Results are averages from resampling (with replacement; 500 times) to address class imbalance. “OA”: overall accuracy.

		Reference									
	Tree type	Healthy	Minor damage	Moderate damage	Major damage	Dead (red)	Dead (gray)	Dead (mixed)	Total	Comm. Err. (%)	User Acc. (%)
Prediction	Healthy	74	4	6	0	0	0	0	84	11.9	88.1
	Minor damage	1	21	14	1	0	0	0	37	43.2	56.8
	Moderate damage	0	0	42	5	6	11	4	68	38.2	61.8
	Major damage	0	0	0	10	2	7	4	23	56.5	43.5
	Dead (red)	0	0	0	0	1	0	0	1	0.0	100.0
	Dead (gray)	0	0	0	0	0	0	0	0	-	-
	Dead (mixed)	0	0	0	0	0	0	5	5	0.0	100.0
	Total	75	25	62	16	9	18	13	218		
	Omis. Err. (%)	1.3	16.0	32.3	37.5	88.9	100.0	61.5		**OA**	70.2%
	Prod. Acc. (%)	98.7	84.0	67.7	62.5	11.1	0.0	38.5			

Table 3.5. Confusion matrix and accuracy metrics for evaluation of top-kill algorithm to separate "*top-kill*" and "*non-top-kill*" from the subset of "*damaged*" trees. Results are averages from resampling (with replacement; 100 times) to address class imbalance.

		Reference				
	Tree type	Non-top-kill	Top-kill	Total	Commission error (%)	User accuracy (%).
Prediction	Non-top-kill	18	2	20	10.0	90.0
	Top-kill	3	38	41	7.3	92.7
	Total	21	40	61		
	Omission error (%)	14.3	5.0		**Overall accuracy**	91.8%
	Producer accuracy (%)	85.7	95.0			

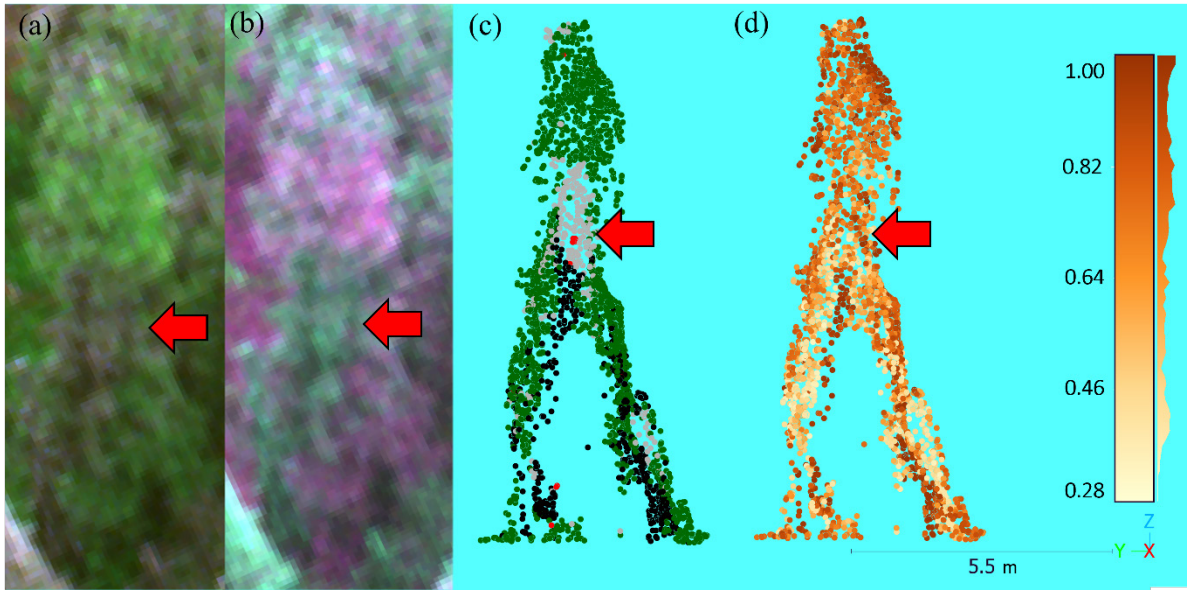

Figure 3.4. Example of branch flagging observed in a tree. (a) True color image. (b) False color image. (c) Random forest model classification; green points are the green class, red is the red class, gray is the gray class, and black is the shadow class. (d) The probability of classes shown in (c); darker colors represent higher probabilities and therefore higher confidence).

3.4 Tree damage across the study site

The RF model applied to the point cloud of the study site reported the classification probability for each point, with 77% of points having a classification probability of 0.75 or higher, indicating that most points were classified with moderate to high confidence. Most points in the green or gray classes were classified with high confidence (Figure 3.5a). Points in the red or gray classes exhibited a range of probabilities greater than 0.4 (Figure 3.5b and c).

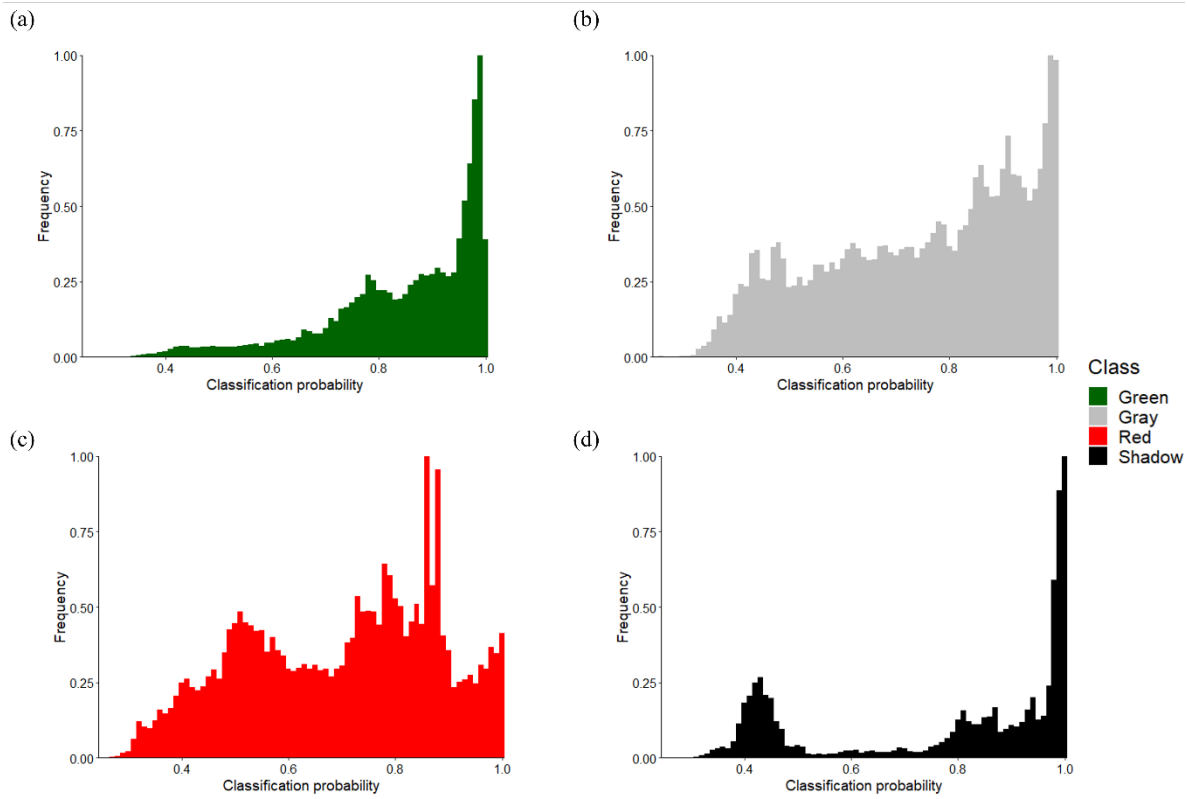

Figure 3.5. Distributions of classification probabilities of points classified as (a) "*green*" class, (b) "*gray*" class, (c) "*red*" class, and (d) "*shadow*" class. Frequencies were normalized by the maximum number of points per bin in each histogram to allow for comparison among classes.

Based on the segmentation results, a total of 15,519 trees occurred across the study site (Table 3.6). Most of the trees were classified as "*healthy*" (78.3%) and the remaining were "*damaged*" (21.7%). A majority of the damaged trees were identified as "*Minor damage*", that is, trees with 5-25% damage points (red plus gray) (58.7%). Among "*damaged*" trees,

most were identified as "*top-kill*" (78.9%); top-kill trees had an average top-kill length of 1.5 m (17.8% of the total tree height on average) (Table 3.6). The "*Dead (mixed)*" class had the highest average length of top-kill (5.8 m), and the "*Dead (gray)*" class had the highest average percentage of top-kill (66.3% of the total tree height).

Table 3.6. Summary of tree-level metrics of healthy and damaged trees, and different damage types across the study site. "TK": top-kill.

Tree type	Num. of trees	Mean % green	Mean % gray	Mean % red	Mean % damage	Num. of Non-TK	Num. of TK	Mean TK length (m)	Mean % TK
Healthy	12143	99.4	0.4	0.3	0.7	-	-	-	-
Damaged	3376	72.1	8.3	19.6	27.9	-	-	-	-
Minor damage	1980	87.6	4.1	8.4	12.4	541	1439	0.9	11.1
Moderate damage	1192	56.3	11.9	31.9	43.8	169	1023	1.7	19.7
Major damage	154	18.3	27.3	54.4	81.7	3	151	4.7	54.7
Dead (red)	5	5.3	91.2	3.5	94.7	0	5	4.8	39.8
Dead (gray)	19	4.6	7.5	87.9	95.4	0	19	4.0	66.3
Dead (mixed)	26	5.0	41.9	53.1	95.0	0	26	5.8	57.9
Total (all trees)	15519	93.4	4.5	2.1	6.6	713	2663	1.5	17.8

Results of the tree segmentation and classification showed good visual agreement when overlaid on the MS orthomosaic (Figure 3.6). Trees identified as "*healthy*" displayed green foliage for a majority of the crown and trees identified as the different damage types showed less green and more gray or red in the crowns (Figure 3.6a). Trees identified as "*top-kill*" with top-kill percentages less than 75% (relative to height of the tree) were apparent with gray tops and green in the lower half of crown for trees and trees identified as "*top-kill*" with greater than 75% top-kill were predominantly gray, red, or mixed in the MS orthomosaic (Figure 3.6b). The probabilities of classification of points, indicating the classification confidence, averaged for each tree were higher on healthy trees (0.78-0.98) compared to damaged trees (0.58-0.68) (Figure 3.6c).

Maps of the study area illustrate the spatial patterns of damage for tree-level data (Figure 3.7) and 30-m resolution (Figure 3.8). For this study area, trees exhibiting moderate to high damage and higher top-kill percentages (51-100%) occurred in distinct clusters (Figure 3.7a and b; Figure 3.8). Most trees were classified with moderate to high confidence (mean tree-level probabilities of 0.58-0.98) (Figure 3.7c). The southern mission (M1) had higher classification confidence than the northern mission (M2) because M1 was comprised of more healthy trees compared with M2, and healthy trees, constituting of predominantly "*green*" classified points, have higher classification confidence than other classes (Figure 3.5a, Figure 3.6c, Figure 3.7c).

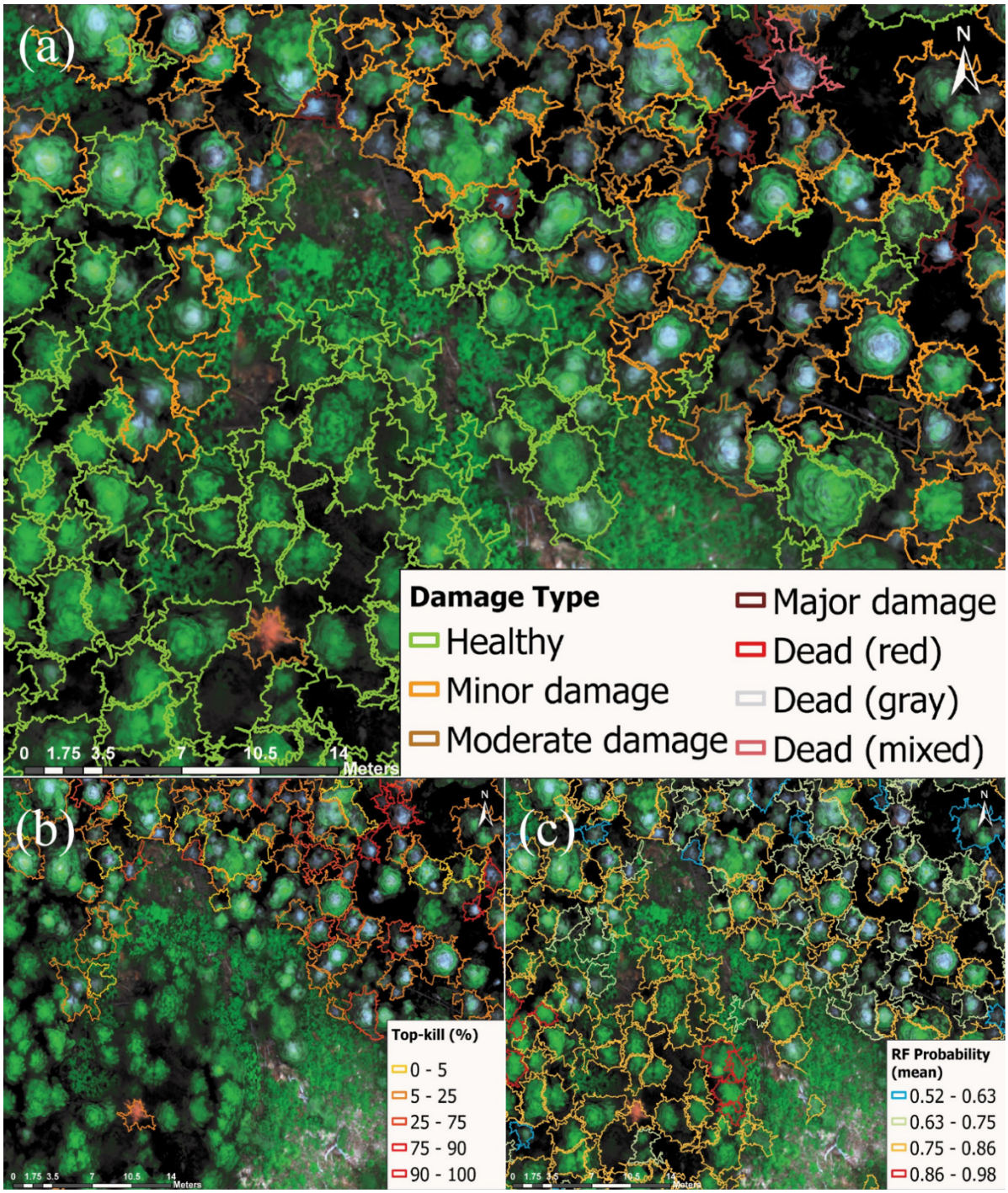

Figure 3.6. Zoomed-in views of tree-level damage metrics for a part of the study site. The basemap imagery is the true color drone orthomosaic (collected using a MicaSense MX-RedEdge sensor). Polygons delineate the crown of individual trees. (a) Damage type identification. (b) Percentage of top-kill relative to tree height for trees identified as "*top-kill*". Trees identified as "*healthy*" or "*non-top-kill*" are not outlined. (c) Average probability of point-level classifications for each tree.

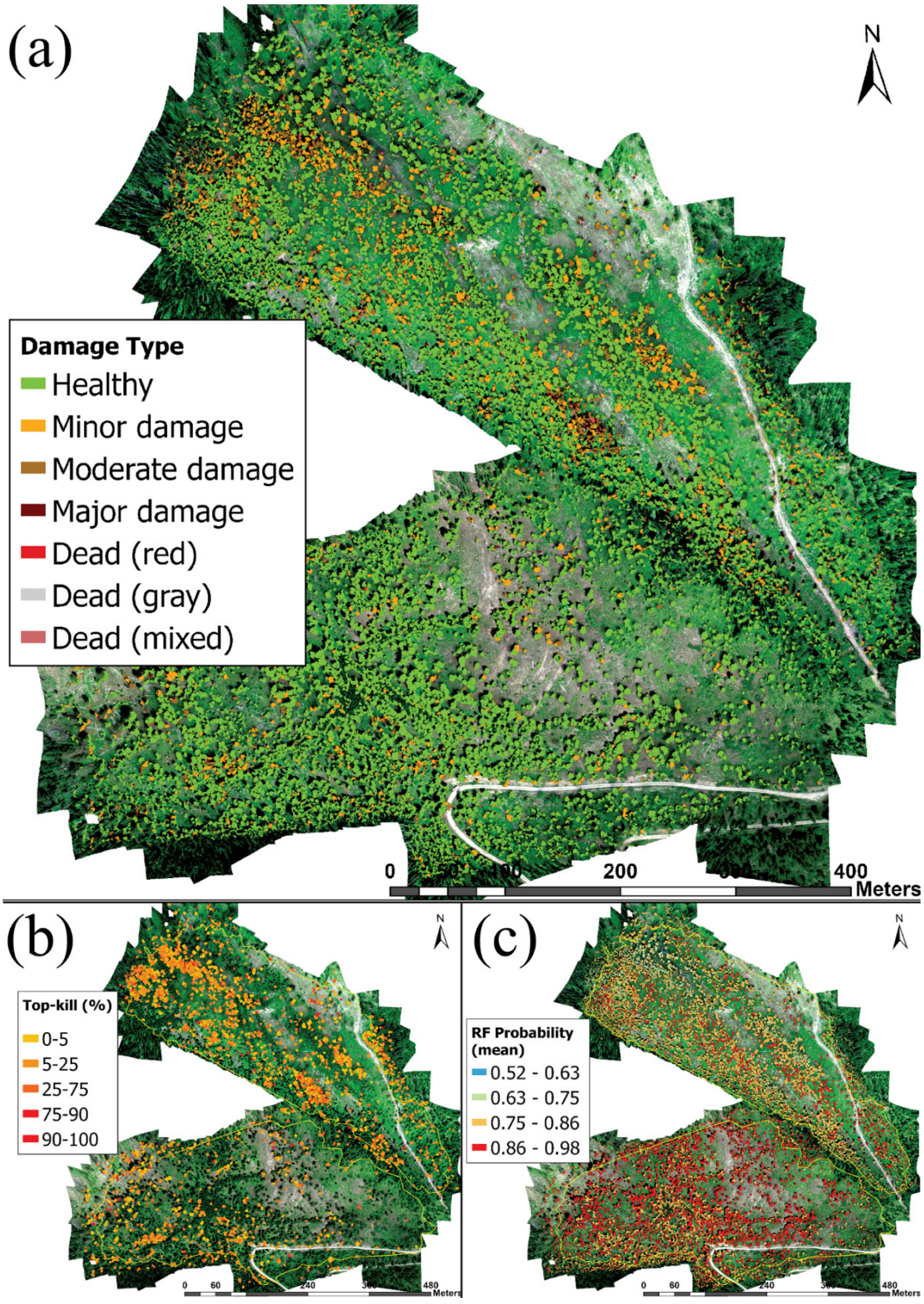

Figure 3.7. Tree-level damage metrics for the study area. Polygons cover the crown of each tree. The basemap imagery is the true color drone orthomosaic (collected using a MicaSense MX-RedEdge sensor). (a) Damage type identification. (b) Percentage of top-kill relative to tree height for trees identified as "*top-kill*". Trees identified as "*healthy*" or "*non-top-kill*" are not outlined. (c) Average probability of classification for all points in each tree.

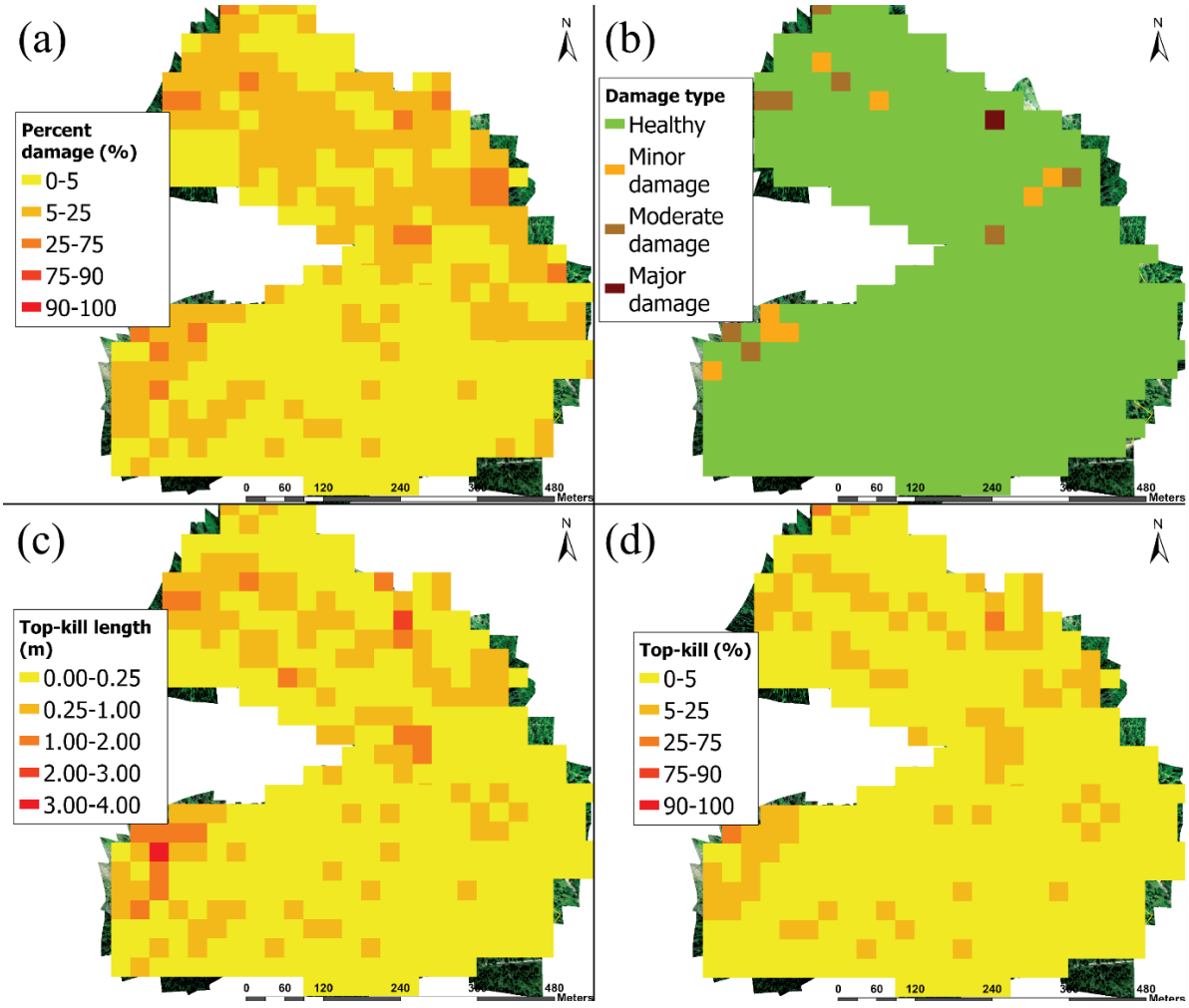

Figure 3.8. Spatially aggregated maps (30-m spatial resolution) produced from tree-level damage maps. (a) Mean percentage of damage (red plus gray) for trees within the grid cell. (b) Modal damage type of trees within the grid cell. (c) Mean top-kill length (m) for top-kill trees within the grid cell. The first class (0.00-0.25) indicates grid cells with predominantly healthy or non-top-kill trees. (d) Mean percentage of top-kill relative to the tree height within the grid cell.

4. Discussion

This study aimed to classify the health status of trees from multispectral reflectances while retaining the 3D information, thereby allowing analyses that consider the vertical location and extent of damage within a tree crown. I established a novel approach that analyzes tree health status in a 3D environment by classifying each point in the point cloud (point-level classification of health status) then classifying the group of points that form trees (tree-level damage algorithm and calculation of damage metrics). Although past studies incorporated structural information when mapping insect-caused damage (Abdollahnejad and Panagiotidis, 2020; Cessna et al., 2021), they did not assess the vertical distribution of damage, which allows a more refined estimate of tree damage.

Accuracies of tree-level damage algorithms are dependent on the performance of the tree segmentation. For this study, the performance of the tree segmentation was similar to other studies that used a point cloud for tree. The accuracy assessment indicated that the primary issue was not in identifying trees, instead, most of the issues arose from the algorithm dividing trees into multiple segments (over-segmentation); only four out of 1000 accuracy assessment points were misclassified as ground. segmentation (Ahmadi et al., 2022; Minařík et al., 2020; Sparks et al., 2022). Additionally, the use of Sørensen's coefficient (SC) showed high spatial agreement with the areas of tree crowns from the reference data set and the crowns delineated by the tree segmentation.

The final RF model was chosen based on the model's overall accuracy (OA) and a visual assessment of the ability to capture the health condition of trees in case studies. The final RF model had high OA and included RBI, NDVI, and REDEDGE as predictor variables. The NDVI and REDEDGE spectral indices are commonly used in vegetation signal detection especially in tree health studies (Guimarães et al., 2020; Hall et al., 2016; Lausch et al., 2016). Models using predictor variables (indices and bands) from only visible bands yielded high accuracies, indicating the effectiveness of this methodology without needing NIR, REDEDGE and related indices, and the potential application using drones with only RGB sensors.

The RF model classified points into "*green*", "*gray*", and "*red*" classes with a classification confidence ranging from moderate to high. Visual assessment of the point cloud of reference trees indicated that points with lower RF confidence occurred in localized areas on tree crown with a mix of green, gray, and red points (an example shown in Figure 3.3). Difficulties in assessing damage within highly localized areas on tree crowns occur in field surveys as well. Studies of observer errors from field surveys assessing defoliation and discoloration (Gertner and Köhl, 1995) and overall tree health (Metzger and Oren, 2001) have demonstrated the inconsistencies in needle damage estimates due to factors such as number of surveyors present (Gertner and Köhl, 1995) and view angle of assessment (Metzger and Oren, 2001).

The first step of the tree damage algorithm, which separated "*healthy*" and "*damaged trees*", had high overall accuracy; the second step, which separated damage types, had reduced accuracy (as expected). RS studies mapping healthy and damaged trees using fine-resolution drone imagery have reported similarly high overall accuracies (Jemaa et al., 2023; Otsu et al., 2019; Zhang et al., 2020). Furthermore, similar moderate overall accuracies have been reported when mapping different damage types, including classification of tree-level health status (Guerra-Hernández et al., 2021; Leidemer et al., 2022) and estimation of damage severity (Cardil et al., 2017; Meng et al., 2018).

Some confusion occurred between the "*Minor damage*", and "*Moderate damage*" classes. The misclassification of "*Minor damage*" trees as "*Moderate damage* " trees (and vice-versa) were due to the trees being slightly under or over the percent damage threshold that separates the two damage types. Sensitivity tests of increasing or decreasing the percent damage threshold resulted in no overall improvement.

Based on the inspection of point clouds of trees identified as "*Dead*" in the reference data set, the confusion between trees identified as one of the "*Dead*" classes ("*red*", "*gray*", "*mixed*") and "*Moderate*" and "*Major*" damaged trees resulted from green points present in the middle or bottom one-half of the *"Dead*" trees (Figure H4). This situation caused the damage assessment algorithm to misidentify the damage type of the tree. The SfM algorithm searches for reoccurring features in multiple drone images to estimate a feature's (e.g., a branch's) position in three-dimensional space (Agisoft Metashape, 2023; Westoby et al., 2012). In the

case of "*Dead*" trees, the algorithm could have experienced difficulties in separating the relatively thin branches from the herbaceous understory or foliage of surrounding trees. As a result, reflectance values from the herbaceous understory or foliage of surrounding trees might have been misassigned to points in the "*Dead*" trees, leading to green points present in the "*Dead*" trees. Similar difficulties in classifying "*Dead*" trees have been reported by studies using computer-vision based approaches to classify tree damage in two-dimensional products (Naseri et al., 2023; Puliti and Astrup, 2022).

The third step of the tree damage algorithm separated all "*damaged*" trees into "*non-top-kill*" and "*top-kill*" with high accuracy. As an outcome of this algorithm, we considered calculating the uncompacted live crown ratio, a metric used for the field-based assessment of tree crown health (Randolph, 2011) computed as the length of live crown relative to the height of the tree. However, estimating the crown base height in this study proved challenging. Qualitative visual assessments of SfM point clouds of trees did not reveal distinct features that could be used to identify the base of the live crown. The absence of points near the crown base in the SfM point cloud did not consistently correspond to the crown base compared to drone images (Figure H5). This absence of points could be attributed to the occlusion of the crown base by neighboring trees in multiple drone images, resulting in an insufficient number of tie-points (recurring features in multiple images), and therefore failing to construct points for the feature (crown base) (Agisoft Metashape, 2023; Westoby et al., 2012).

Application of the tree-level damage algorithm across the study area identified most trees as "*healthy*" and the rest as "*damaged*" with moderate to high confidence. Most of the "*damaged*" trees in the study area were "*top-kill*" trees with an average damage of less than a quarter of the tree from the treetop downward, "*dead*" trees had the largest average length of top-kill spanning more than three-quarters of the height of the tree from the treetop downward. Some trees showed signs of branch flagging (Figure 3.4), suggesting a potential for the use of these data and methods for identifying such trees. Tree-level damage maps of the study area showed clusters of tree damage, demonstrating the feasibility of utilizing point cloud to map tree damage and produce tree-level damage metrics (Figure 3.6, Figure 3.7, Figure 3.8).

The spatially aggregated maps produced in this study demonstrate the capability to generate spatially upscaled data products, moving from a tree-level scale to a medium-resolution satellite data scale (e.g., Landsat). This spatial upscaling facilitates the integration of tree-level products from drones with satellite data, which is useful for mapping of forests (Fassnacht et al., 2023) and developing and testing of ecological models to inform management decisions (Masek et al., 2015). The results produced in this study demonstrate the ability of drones to bridge the gap between field-based forest inventory methods and space-based remote sensing of forests to aid in research and management – a role that has been highlighted in multiple reviews of forest remote sensing (Ecke et al., 2022; Fassnacht et al., 2023; Lausch et al., 2017).

5. Conclusion

This study describes a novel method for detecting insect-caused damage on parts of individual trees. I developed a model to identify damage for points in three-dimensional space, thereby enabling the identification of damage locations within crowns. Subsequently, I developed, evaluated, and applied an algorithm for separating trees into healthy, damaged, and different damage types, and for analyzing damaged trees for top-kill. Top-kill is characteristic of certain forest insects, such as DFTM and WSBW, and might be used to differentiate damage from defoliators from bark beetles (Ciesla et al., 2015; Fellin and Dewey, 1986; Ferrell, 1986; Hall et al., 2016, 2006). Thus, these methods can not only refine estimates of where damage is located on individual trees but also have the potential for improving attribution of damage to insect species or types.

The algorithms developed here from drone imagery can be applied using point clouds derived from data from other platforms as well. Recent studies have utilized NAIP imagery in constructing point clouds for forestry inventory estimates (Ritz et al., 2022; Schroeder et al., 2022). In addition, the methodology can be applied using multispectral LiDAR systems that simultaneously collect active RS data in multiple wavelengths (Budei et al., 2021; Ekhtari et al., 2018). However, it is important to consider the financial implications of acquiring LiDAR sensors and LiDAR-capable systems. Exploring the capability of SfM point clouds using less expensive sensors was one of the motivations behind this project.

Future directions could focus on ecological applications in management and research. The methods of estimating three-dimensional tree damage described here can be used to examine impacts of snow interception (Russell et al., 2021; Storck et al., 2002), habitat availability (Dial et al., 2004; Leiterer et al., 2015), tree canopy volume estimations (Di Gennaro and Matese, 2020), and carbon stocks (Bright et al. 2012).

The data products and maps produced in this study demonstrate the utilization of a SfM-derived point cloud from drone imagery in successfully mapping 3D damage on trees and estimating top-kill. This study advances the current understanding of the potential and limitations of using SfM-derived point cloud in top-kill detection. The methods developed in

this study can be applied to improve monitoring and mapping forest insect and disease damage.

References

Abdollahnejad, A., Panagiotidis, D., 2020. Tree Species Classification and Health Status Assessment for a Mixed Broadleaf-Conifer Forest with UAS Multispectral Imaging. Remote Sensing 12, 3722. https://doi.org/10.3390/rs12223722

Aber, J.S., 2019. Small-format aerial photography and UAS imagery : principles, techniques, and geoscience applications, Second edition. ed, Small-format aerial photography and UAS imagery : principles, techniques, and geoscience applications. Elsevier, Burlington, Vermont.

Agisoft Metashape, 2023. Agisoft Metashape User Manual - Professional Edition, Version 2.0. Copyright © 2023 Agisoft LLC.

Ahmadi, S.A., Ghorbanian, A., Golparvar, F., Mohammadzadeh, A., Jamali, S., 2022. Individual tree detection from unmanned aerial vehicle (UAV) derived point cloud data in a mixed broadleaf forest using hierarchical graph approach. European Journal of Remote Sensing 55, 520–539. https://doi.org/10.1080/22797254.2022.2129095

Anderegg, W.R.L., Hicke, J.A., Fisher, R.A., Allen, C.D., Aukema, J., Bentz, B., Hood, S., Lichstein, J.W., Macalady, A.K., McDowell, N., Pan, Y., Raffa, K., Sala, A., Shaw, J.D., Stephenson, N.L., Tague, C., Zeppel, M., 2015. Tree mortality from drought, insects, and their interactions in a changing climate. New Phytologist 208, 674–683. https://doi.org/10.1111/nph.13477

Anderegg, W.R.L., Trugman, A.T., Badgley, G., Anderson, C.M., Bartuska, A., Ciais, P., Cullenward, D., Field, C.B., Freeman, J., Goetz, S.J., Hicke, J.A., Huntzinger, D., Jackson, R.B., Nickerson, J., Pacala, S., Randerson, J.T., 2020. Climate-driven risks to the climate mitigation potential of forests. Science 368, eaaz7005. https://doi.org/10.1126/science.aaz7005

Arneth, A., Denton, F., Agus, F., Elbehri, A., Erb, K.H., Elasha, B.O., Rahimi, M., Rounsevell, M., Spence, A., Valentini, R., others, 2019. Framing and context, in: Climate Change and Land: An IPCC Special Report on Climate Change, Desertification, Land Degradation, Sustainable Land Management, Food Security, and Greenhouse Gas Fluxes in Terrestrial Ecosystems. Intergovernmental Panel on Climate Change (IPCC), pp. 1–98.

ASPRS, A.S. for P. and R.S., 2019. LAS Specification 1.4-R15.

Barbeito, I., Dassot, M., Bayer, D., Collet, C., Drössler, L., Löf, M., del Rio, M., Ruiz-Peinado, R., Forrester, D.I., Bravo-Oviedo, A., Pretzsch, H., 2017. Terrestrial laser scanning reveals differences in crown structure of Fagus sylvatica in mixed vs. pure European forests. Forest Ecology and Management 405, 381–390. https://doi.org/10.1016/j.foreco.2017.09.043

Bentz, B.J., Régnière, J., Fettig, C.J., Hansen, E.M., Hayes, J.L., Hicke, J.A., Kelsey, R.G., Negrón, J.F., Seybold, S.J., 2010. Climate Change and Bark Beetles of the Western United States and Canada: Direct and Indirect Effects. BioScience 60, 602–613. https://doi.org/10.1525/bio.2010.60.8.6

Breiman, L., 2001. Random Forests. Machine Learning 45, 5–32. https://doi.org/10.1023/A:1010933404324

Bright, B.C., Hicke, J.A., Hudak, A.T., 2012. Estimating aboveground carbon stocks of a forest affected by mountain pine beetle in Idaho using lidar and multispectral imagery. Remote Sensing of Environment 124, 270–281. https://doi.org/10.1016/j.rse.2012.05.016

Budei, B.C., St-Onge, B., Fournier, R.A., Kneeshaw, D., 2021. Effect of variability of normalized differences calculated from multi-spectral lidar on individual tree species identification, . pp. 188–190.

Cardil, A., Otsu, K., Pla, M., Silva, C.A., Brotons, L., 2019. Quantifying pine processionary moth defoliation in a pine-oak mixed forest using unmanned aerial systems and multispectral imagery. PLoS ONE 14, e0213027. https://doi.org/10.1371/journal.pone.0213027

Cardil, A., Vepakomma, U., Brotons, L., 2017. Assessing Pine Processionary Moth Defoliation Using Unmanned Aerial Systems. Forests 8, 402. https://doi.org/10.3390/f8100402

Cessna, J., Alonzo, M.G., Foster, A.C., Cook, B.D., 2021. Mapping Boreal Forest Spruce Beetle Health Status at the Individual Crown Scale Using Fused Spectral and Structural Data. Forests 12, 1145. https://doi.org/10.3390/f12091145

Ciesla, W.M., Stephens, S.S., Brian E Howell, Backsen, J.C., 2015. Aerial Signatures of Forest Damage in Colorado and Adjoining States 142.

Clay, G.R., Marsh, S.E., others, 1997. Spectral analysis for articulating scenic color changes in a coniferous landscape. Photogrammetric engineering and remote sensing 63, 1353–1362.

CloudCompare (version 2.12.4), 2022. . GPL Software. Retrieved from http://www.cloudcompare.org/.

Cohen, W.B., Yang, Z., Stehman, S.V., Schroeder, T.A., Bell, D.M., Masek, J.G., Huang, C., Meigs, G.W., 2016. Forest disturbance across the conterminous United States from 1985–2012: The emerging dominance of forest decline. Forest Ecology and Management, Special Section: Forest Management for Climate Change 360, 242–252. https://doi.org/10.1016/j.foreco.2015.10.042

Dainelli, R., Toscano, P., Di Gennaro, S.F., Matese, A., 2021. Recent Advances in Unmanned Aerial Vehicle Forest Remote Sensing—A Systematic Review. Part I: A General Framework. Forests 12, 327. https://doi.org/10.3390/f12030327

Di Gennaro, S.F., Matese, A., 2020. Evaluation of novel precision viticulture tool for canopy biomass estimation and missing plant detection based on 2.5 D and 3D approaches using RGB images acquired by UAV platform. Plant Methods 16, 1–12.

Dial, R., Bloodworth, B., Lee, A., Boyne, P., Heys, J., 2004. The Distribution of Free Space and Its Relation to Canopy Composition at Six Forest Sites. Forest Science 50, 312–325. https://doi.org/10.1093/forestscience/50.3.312

Dowle, M., Srinivasan, A., 2023. data.table: Extension of `data.frame`.

Duarte, A., Borralho, N., Cabral, P., Caetano, M., 2022. Recent Advances in Forest Insect Pests and Diseases Monitoring Using UAV-Based Data: A Systematic Review. Forests 13, 911. https://doi.org/10.3390/f13060911

Ecke, S., Dempewolf, J., Frey, J., Schwaller, A., Endres, E., Klemmt, H.-J., Tiede, D., Seifert, T., 2022. UAV-Based Forest Health Monitoring: A Systematic Review. Remote Sensing 14, 3205. https://doi.org/10.3390/rs14133205

Ekhtari, N., Glennie, C., Fernandez-Diaz, J.C., 2018. Classification of Airborne Multispectral Lidar Point Clouds for Land Cover Mapping. IEEE Journal of Selected Topics in Applied Earth Observations and Remote Sensing 11, 2068–2078. https://doi.org/10.1109/JSTARS.2018.2835483

Fang, F., Im, J., Lee, J., Kim, K., 2016. An improved tree crown delineation method based on live crown ratios from airborne LiDAR data. GIScience & Remote Sensing 53, 402–419. https://doi.org/10.1080/15481603.2016.1158774

Fassnacht, F.E., White, J.C., Wulder, M.A., Næsset, E., 2023. Remote sensing in forestry: current challenges, considerations and directions. Forestry: An International Journal of Forest Research cpad024.

Fellin, D.G.;, Dewey, J.E., 1986. Western Spruce Budworm Forest Insect & Disease Leaflet. Forest Insect & Disease Leaflet 53 (revised). USDA Forest Service, Washington, D. C 10.

Ferrell, G.T., 1986. Fir Engraver Forest Insect & Disease Leaflet. Forest Insect & Disease Leaflet 13 (revised). USDA Forest Service, Washington, D. C 8.

Gamon, J.A., Surfus, J.S., 1999. Assessing leaf pigment content and activity with a reflectometer. The New Phytologist 143, 105–117. https://doi.org/10.1046/j.1469-8137.1999.00424.x

Gertner, G., Köhl, M., 1995. Correlated Observer Errors and their Effects on Survey Estimates of Needle-Leaf Loss. Forest Science 41, 758–776.

Graham, M.H., 2003. Confronting multicollinearity in ecological multiple regression. Ecology 84, 2809–2815.

Guerra-Hernández, J., Díaz-Varela, R.A., Ávarez-González, J.G., Rodríguez-González, P.M., 2021. Assessing a novel modelling approach with high resolution UAV imagery for monitoring health status in priority riparian forests. For. Ecosyst. 8, 61. https://doi.org/10.1186/s40663-021-00342-8

Guimarães, N., Pádua, L., Marques, P., Silva, N., Peres, E., Sousa, J.J., 2020. Forestry Remote Sensing from Unmanned Aerial Vehicles: A Review Focusing on the Data, Processing and Potentialities. Remote Sensing 12, 1046. https://doi.org/10.3390/rs12061046

Hall, R.J., Castilla, G., White, J.C., Cooke, B.J., Skakun, R.S., 2016. Remote sensing of forest pest damage: a review and lessons learned from a Canadian perspective. Can Entomol 148, S296–S356. https://doi.org/10.4039/tce.2016.11

Hall, R.J., Skakun, R., Arsenault, E., 2006. Remotely Sensed Data in the Mapping of Insect Defoliation. https://doi.org/10.1201/9781420005189.ch4

Hall, R.J., Volney, W., Wang, Y., 1998. Using a geographic information system (GIS) to associate forest stand characteristics with top kill due to defoliation by the jack pine budworm. Can. J. For. Res. 28, 1317–1327. https://doi.org/10.1139/x98-108

Hardin, P.J., Shumway, J.M., 1997. Statistical Significance and Normalized Confusion Matrices.

Hartmann, H., Bastos, A., Das, A.J., Esquivel-Muelbert, A., Hammond, W.M., Martínez-Vilalta, J., McDowell, N.G., Powers, J.S., Pugh, T.A.M., Ruthrof, K.X., Allen, C.D., 2022. Climate Change Risks to Global Forest Health: Emergence of Unexpected Events of Elevated Tree Mortality Worldwide. Annu. Rev. Plant Biol. 73, 673–702. https://doi.org/10.1146/annurev-arplant-102820-012804

Hicke, J.A., Lucatello, S., Mortsch, L.D., Dawson, J., Aguilar, M.D., Enquist, C.A.F., Gilmore, E.A., Gutzler, D.S., Harper, S., Holsman, K., Jewett, E.B., Kohler, T.A., Miller, K., 2022. North America (Assessment Report No. Sixth), Climate Change 2022: Impacts, Adaptation and Vulnerability. Intergovernmental Panel on Climate Change.

Hicke, J.A., Meddens, A.J.H., Kolden, C.A., 2016. Recent Tree Mortality in the Western United States from Bark Beetles and Forest Fires. Forest Science 62, 141–153. https://doi.org/10.5849/forsci.15-086

Hijmans, R.J., Bivand, R., Pebesma, E., Sumner, M.D., 2023. terra: Spatial Data Analysis.

Hunt Jr., E.R., Daughtry, C.S.T., Eitel, J.U.H., Long, D.S., 2011. Remote Sensing Leaf Chlorophyll Content Using a Visible Band Index. Agronomy Journal 103, 1090–1099. https://doi.org/10.2134/agronj2010.0395

James, M.R., Robson, S., d'Oleire-Oltmanns, S., Niethammer, U., 2017. Optimising UAV topographic surveys processed with structure-from-motion: Ground control quality, quantity and bundle adjustment. Geomorphology 280, 51–66. https://doi.org/10.1016/j.geomorph.2016.11.021

Jemaa, H., Bouachir, W., Leblon, B., LaRocque, A., Haddadi, A., Bouguila, N., 2023. UAV-Based Computer Vision System for Orchard Apple Tree Detection and Health Assessment. Remote Sensing 15, 3558. https://doi.org/10.3390/rs15143558

Jensen, J.R., 2016. Introductory digital image processing : a remote sensing perspective, 4th Edition. ed, Introductory digital image processing : a remote sensing perspective, Pearson series in geographic information science. Pearson Education, Inc., Glenview, IL.

Lausch, A., Erasmi, S., King, D., Magdon, P., Heurich, M., 2017. Understanding Forest Health with Remote Sensing-Part II—A Review of Approaches and Data Models. Remote Sensing 9, 129. https://doi.org/10.3390/rs9020129

Lausch, A., Erasmi, S., King, D., Magdon, P., Heurich, M., 2016. Understanding Forest Health with Remote Sensing -Part I—A Review of Spectral Traits, Processes and Remote-Sensing Characteristics. Remote Sensing 8, 1029. https://doi.org/10.3390/rs8121029

Legendre, P., Legendre, L., others, 1998. Numerical ecology: developments in environmental modelling. Developments in Environmental Modelling 20.

Leidemer, T., Gonroudobou, O.B.H., Nguyen, H.T., Ferracini, C., Burkhard, B., Diez, Y., Lopez Caceres, M.L., 2022. Classifying the Degree of Bark Beetle-Induced Damage on Fir (Abies mariesii) Forests, from UAV-Acquired RGB Images. Computation 10, 63. https://doi.org/10.3390/computation10040063

Leiterer, R., Furrer, R., Schaepman, M.E., Morsdorf, F., 2015. Forest canopy-structure characterization: A data-driven approach. Forest Ecology and Management 358, 48–61. https://doi.org/10.1016/j.foreco.2015.09.003

Li, W., Guo, Q., Jakubowski, M.K., Kelly, M., 2012. A New Method for Segmenting Individual Trees from the Lidar Point Cloud. photogramm eng remote sensing 78, 75–84. https://doi.org/10.14358/PERS.78.1.75

Liaw, A., Wiener, M., 2002. Classification and Regression by randomForest. R News 2, 18–22.

Luo, Y., Huang, H., Roques, A., 2023. Early Monitoring of Forest Wood-Boring Pests with Remote Sensing. Annual Review of Entomology 68, 277–298. https://doi.org/10.1146/annurev-ento-120220-125410

Malley, J.D., Kruppa, J., Dasgupta, A., Malley, K.G., Ziegler, A., 2012. Probability Machines. Methods Inf Med 51, 74–81. https://doi.org/10.3414/ME00-01-0052

Masek, J.G., Hayes, D.J., Joseph Hughes, M., Healey, S.P., Turner, D.P., 2015. The role of remote sensing in process-scaling studies of managed forest ecosystems. Forest Ecology and Management, Carbon, water and nutrient cycling in managed forests 355, 109–123. https://doi.org/10.1016/j.foreco.2015.05.032

Meng, R., Dennison, P.E., Zhao, F., Shendryk, I., Rickert, A., Hanavan, R.P., Cook, B.D., Serbin, S.P., 2018. Mapping canopy defoliation by herbivorous insects at the individual tree level using bi-temporal airborne imaging spectroscopy and LiDAR measurements. Remote Sensing of Environment 215, 170–183. https://doi.org/10.1016/j.rse.2018.06.008

Metzger, J.M., Oren, R., 2001. The Effect of Crown Dimensions on Transparency and the Assessment of Tree Health. Ecological Applications 11, 1634–1640. https://doi.org/10.1890/1051-0761(2001)011[1634:TEOCDO]2.0.CO;2

MicaSense, Inc, 2023. RedEdge-MX Integration Guide [WWW Document]. MicaSense Knowledge Base. URL https://support.micasense.com/hc/en-us/articles/360011389334-RedEdge-MX-Integration-Guide (accessed 1.14.23).

Minařík, R., Langhammer, J., Lendzioch, T., 2020. Automatic Tree Crown Extraction from UAS Multispectral Imagery for the Detection of Bark Beetle Disturbance in Mixed Forests. Remote Sensing 12, 4081. https://doi.org/10.3390/rs12244081

Mohan, M., Leite, R.V., Broadbent, E.N., Jaafar, W.S.W.M., Srinivasan, S., Bajaj, S., Corte, A.P.D., Amaral, C.H. do, Gopan, G., Saad, S.N.M., Kamarulzaman, A.M.M., Prata, G.A., Llewelyn, E., Johnson, D.J., Doaemo, W., Bohlman, S., Zambrano, A.M.A., Cardil, A., 2021. Individual tree detection using UAV-lidar and UAV-SfM data: A tutorial for beginners. Open Geosciences 13, 1028–1039. https://doi.org/10.1515/geo-2020-0290

Naseri, M.H., Shataee Jouibary, S., Habashi, H., 2023. Analysis of forest tree dieback using UltraCam and UAV imagery. Scandinavian Journal of Forest Research 1–9.

NOAA, 2021. NOAA NCEI U.S. Climate Normals Quick Access [WWW Document]. URL https://www.ncei.noaa.gov/access/us-climate-normals/#dataset=normals-annualseasonal&timeframe=30&location=MT&station=USW00024153 (accessed 9.28.23).

Otsu, K., Pla, M., Duane, A., Cardil, A., Brotons, L., 2019. Estimating the Threshold of Detection on Tree Crown Defoliation Using Vegetation Indices from UAS Multispectral Imagery. Drones 3, 80. https://doi.org/10.3390/drones3040080

Otsu, K., Pla, M., Vayreda, J., Brotons, L., 2018. Calibrating the Severity of Forest Defoliation by Pine Processionary Moth with Landsat and UAV Imagery. Sensors 18, 3278. https://doi.org/10.3390/s18103278

Pearce, D.W., 2001. The Economic Value of Forest Ecosystems. Ecosystem Health 7, 284–296. https://doi.org/10.1046/j.1526-0992.2001.01037.x

Pederson, L.E., Lowrey, T.;, Bulaon, L.;, B., 2020. Douglas-fir Tussock Moth. Forest Insect & Disease Leaflet. Forest Insect & Disease Leaflet 86 (revised). USDA Forest Service, Washington, D.C 86.

Perez, D., Lu, Y., Kwan, C., Shen, Y., Koperski, K., Li, J., 2018. Combining Satellite Images with Feature Indices for Improved Change Detection, in: 2018 9th IEEE Annual Ubiquitous Computing, Electronics & Mobile Communication Conference (UEMCON). Presented at the 2018 9th IEEE Annual Ubiquitous Computing, Electronics & Mobile Communication Conference (UEMCON), pp. 438–444. https://doi.org/10.1109/UEMCON.2018.8796538

Photogrammetry, A.S. for, Sensing, R., 2019. LAS Specification 1.4-R15.

Puliti, S., Astrup, R., 2022. Automatic detection of snow breakage at single tree level using YOLOv5 applied to UAV imagery. International Journal of Applied Earth Observation and Geoinformation 112, 102946. https://doi.org/10.1016/j.jag.2022.102946

Pureswaran, D.S., Roques, A., Battisti, A., 2018. Forest Insects and Climate Change. Curr Forestry Rep 4, 35–50. https://doi.org/10.1007/s40725-018-0075-6

Qi, Y., 2012. Random Forest for Bioinformatics, in: Zhang, C., Ma, Y. (Eds.), Ensemble Machine Learning: Methods and Applications. Springer, New York, NY, pp. 307–323. https://doi.org/10.1007/978-1-4419-9326-7_11

Randolph, K., 2011. USDA Forest Service FIA Phase 3 field guide. Crowns: measurements and sampling.

Rhodes, M.W., Bennie, J.J., Spalding, A., ffrench-Constant, R.H., Maclean, I.M.D., 2022. Recent advances in the remote sensing of insects. Biological Reviews 97, 343–360. https://doi.org/10.1111/brv.12802

Ritz, A.L., Thomas, V.A., Wynne, R.H., Green, P.C., Schroeder, T.A., Albaugh, T.J., Burkhart, H.E., Carter, D.R., Cook, R.L., Campoe, O.C., Rubilar, R.A., Rakestraw, J., 2022. Assessing the utility of NAIP digital aerial photogrammetric point clouds for estimating canopy height of managed loblolly pine plantations in the southeastern United States. Int. J. Appl. Earth Obs. Geoinf. 113, 103012. https://doi.org/10.1016/j.jag.2022.103012

Rouse, J.W., Haas, R.H., Schell, J.A., Deering, D.W., 1974. Monitoring vegetation systems in the Great Plains with ERTS.

Roussel, J.-R., Auty, D., Coops, N.C., Tompalski, P., Goodbody, T.R.H., Meador, A.S., Bourdon, J.-F., Boissieu, F. de, Achim, A., 2020. lidR: An R package for analysis of Airborne Laser Scanning (ALS) data. Remote Sensing of Environment 251, 112061. https://doi.org/10.1016/j.rse.2020.112061

Roussel, J.-R., documentation), D.A. (Reviews the, features), F.D.B. (Fixed bugs and improved catalog, segment_snags()), A.S.M. (Implemented wing2015() for, track_sensor()), B.J.-F. (Contributed to R. for, track_sensor()), G.D. (Implemented G. for, management), L.S. (Contributed to parallelization, code), S.A. (Author of the C. concaveman, 2022. lidR: Airborne LiDAR Data Manipulation and Visualization for Forestry Applications.

Russell, M., Eitel, J.U.H., Link, T.E., Silva, C.A., 2021. Important Airborne Lidar Metrics of Canopy Structure for Estimating Snow Interception. Remote Sensing 13, 4188. https://doi.org/10.3390/rs13204188

Schloerke, B., Cook, D., Larmarange, J., Briatte, F., Marbach, M., Thoen, E., Elberg, A., Toomet, O., Crowley, J., Hofmann, H., Wickham, H., 2023. GGally: Extension to "ggplot2."

Schroeder, T.A., Obata, S., Papeş, M., Branoff, B., 2022. Evaluating Statewide NAIP Photogrammetric Point Clouds for Operational Improvement of National Forest Inventory Estimates in Mixed Hardwood Forests of the Southeastern U.S. Remote Sensing 14, 4386. https://doi.org/10.3390/rs14174386

Senf, C., Seidl, R., Hostert, P., 2017. Remote sensing of forest insect disturbances: Current state and future directions. International Journal of Applied Earth Observation and Geoinformation 60, 49–60. https://doi.org/10.1016/j.jag.2017.04.004

Silva, C.A., Hudak, A.T., Vierling, L.A., Loudermilk, E.L., O'Brien, J.J., Hiers, J.K., Jack, S.B., Gonzalez-Benecke, C., Lee, H., Falkowski, M.J., Khosravipour, A., 2016. Imputation of Individual Longleaf Pine (Pinus palustris Mill.) Tree Attributes from Field and LiDAR Data. Canadian Journal of Remote Sensing 42, 554–573. https://doi.org/10.1080/07038992.2016.1196582

Sparks, A.M., Corrao, M.V., Smith, A.M.S., 2022. Cross-Comparison of Individual Tree Detection Methods Using Low and High Pulse Density Airborne Laser Scanning Data. Remote Sensing 14, 3480. https://doi.org/10.3390/rs14143480

Stahl, A.T., Andrus, R., Hicke, J.A., Hudak, A.T., Bright, B.C., Meddens, A.J.H., 2023. Automated attribution of forest disturbance types from remote sensing data: A synthesis. Remote Sensing of Environment 285, 113416. https://doi.org/10.1016/j.rse.2022.113416

Storck, P., Lettenmaier, D.P., Bolton, S.M., 2002. Measurement of snow interception and canopy effects on snow accumulation and melt in a mountainous maritime climate, Oregon, United States. Water Resources Research 38, 5-1-5–16. https://doi.org/10.1029/2002WR001281

Tinkham, W.T., Swayze, N.C., 2021. Influence of Agisoft Metashape Parameters on UAS Structure from Motion Individual Tree Detection from Canopy Height Models. Forests 12, 250. https://doi.org/10.3390/f12020250

Westoby, M.J., Brasington, J., Glasser, N.F., Hambrey, M.J., Reynolds, J.M., 2012. 'Structure-from-Motion' photogrammetry: A low-cost, effective tool for geoscience applications. Geomorphology 179, 300–314. https://doi.org/10.1016/j.geomorph.2012.08.021

Wickman, B., 1979. How to estimate defoliation and predict tree damage [during outbreaks of the Douglas-fir tussock moth, Orgyia pseudotsugata]. Agriculture Handbook-US Dept. of Agriculture (USA). no. 550.

Woebbecke, D.M., Meyer, G.E., Von Bargen, K., Mortensen, D.A., 1995. Color indices for weed identification under various soil, residue, and lighting conditions. Transactions of the ASAE 38, 259–269.

Young, D.J.N., Koontz, M.J., Weeks, J., 2022. Optimizing aerial imagery collection and processing parameters for drone-based individual tree mapping in structurally complex conifer forests. Methods Ecol Evol 13, 1447–1463. https://doi.org/10.1111/2041-210X.13860

Zhang, K., Chen, S.-C., Whitman, D., Shyu, M.-L., Yan, J., Zhang, C., 2003. A progressive morphological filter for removing nonground measurements from airborne LIDAR data. IEEE Transactions on Geoscience and Remote Sensing 41, 872–882. https://doi.org/10.1109/TGRS.2003.810682

Zhang, N., Wang, Y., Zhang, X., 2020. Extraction of tree crowns damaged by Dendrolimus tabulaeformis Tsai et Liu via spectral-spatial classification using UAV-based hyperspectral images. Plant Methods 16, 135. https://doi.org/10.1186/s13007-020-00678-2

Appendix A. Outbreak history of study area and drone mission flight lines

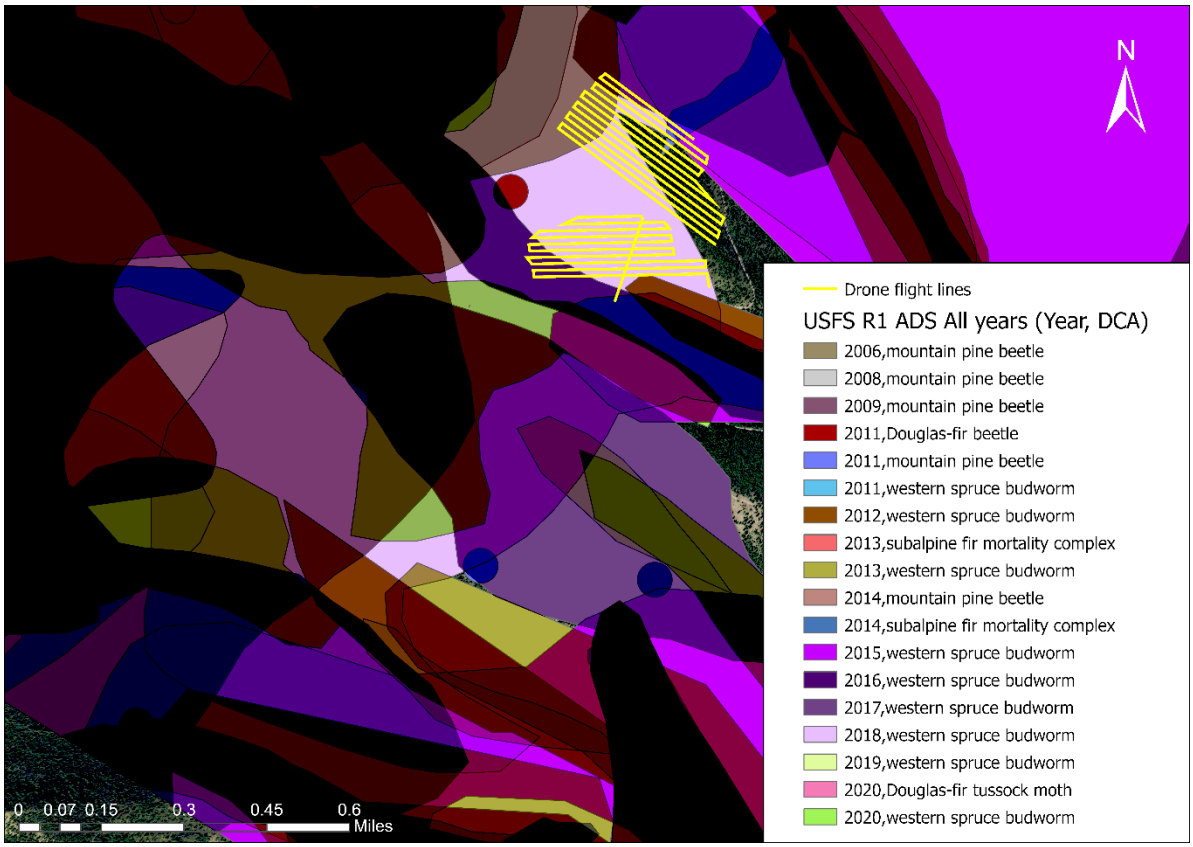

Figure A1. Drone flights (yellow lines) superimposed on polygons from the USDA Forest Service Aerial Detection Surveys showing insect damage from recent years. “DCA”: damage causal agent.

Appendix B. Drone data pre-processing

B.1. GCP marker corrections and point cloud optimization

Table B1. Estimated positional errors (root mean square error, RMSE) from each processing step by drone mission. RMSE values are estimated by Agisoft Metashape accessible via generation of processing reports. The control points and check points are chosen from the pool of available GCP markers for each drone mission site.

Processing stage	Mission	X error (m)	Y error (m)	Z error (m)	Total error (m)
RTK-GNSS error	M1	2.04	0.68	0.48	2.20
	M2	1.66	1.10	1.76	2.66
	Mean	1.85	0.89	1.12	2.43
Final product fit (control points RMSE)	M1	0.12	0.25	0.20	0.35
	M2	0.01	0.01	0.05	0.05
	Mean	0.07	0.13	0.13	0.20
Final product accuracy (check points RMSE)	M1	0.02	0.09	0.03	0.09
	M2	0.01	0.03	0.07	0.07
	Mean	0.02	0.06	0.05	0.08

B.2. Assignment of multispectral reflectance values to SfM point cloud

The MX-RedEdge sensor records data in five spectral bands (MicaSense, Inc, 2023), and these multispectral reflectances can be assigned to the point cloud using the "*Calculate Point Colors*" option in Metashape. However, the American Society for Photogrammetry and Remote Sensing (ASPRS) (2019) specifications for .las format data limit band data storage to only 4 bands while exporting (R, G, B, NIR). Therefore, a workaround was implemented to create a .las point cloud file. The point cloud constructed from the multispectral sensor was exported as a .XYZ file (plain text file) from Agisoft Metashape. The .XYZ point cloud file was imported into CloudCompare (version 2.12.4, https://www.cloudcompare.org/, accessed August 2022) and re-exported as a .las file with the projected coordinate system set to EPSG:26912 (NAD83/UTM Zone 12). During this process, the five-band reflectance data were stored as "*Extra Bytes Variable Length Records (VLR)*" on the .las file (ASPRS, 2019). If future updates to the LAS specifications (ASPRS, 2019) allow for more than four band information storage, then a streamlined export to .las file from Agisoft Metashape is suggested.

The SfM point cloud with multispectral reflectance values was imported into R using the "*lidR*" package (Roussel et al., 2022). The attributes of each point in the point cloud were stored as a "*data.table*" format under the "*@data*" slot of the imported "*LAS-class*" object (Roussel et al., 2022). The "*data.table*" package (Dowle and Srinivasan, 2023) allows for efficient memory allocation and recycling in R and is thus central to data storage and manipulation in the "*lidR*" package (Roussel et al., 2020). Since the "*data.table*" format is an extension of R's native "*data.frame*" class (Dowle and Srinivasan, 2023), the "*data.table*" format was used throughout the project, especially when accessing and updating point cloud data attributes.

Appendix C. Reference data

C.1. Individual drone-captured images

The locations of the reference trees from the manually delineated tree crown polygon layer were exported as a point shapefile to Metashape. The imported reference tree location shapefile was converted to "*markers*", and the "*filter photos by markers*" option was used to view individual drone-captured images that contained the reference trees. This backtracking to individual drone images allowed for the location and evaluation of the damage along the height of the trees as the same tree can be seen in multiple images from different angles. These multi-image evaluations of tree damage were used for qualitative assessments of the random forest classification of points in the point cloud and the separation individual trees into different damage types.

C.2. On-screen selection of points representing green, grey, red, and shadow classes on the point cloud data set.

The point cloud with tree segmentation was loaded into R and an "*ID_point*" attribute was programmatically added to the point cloud data set. The "*ID_point*" attribute represented a unique identification number for each point in the point cloud data set.

The point cloud with the "*ID_point*" attribute was imported into CloudCompare with the reference trees polygon layer from ArcGIS (Figure C1a). The "*point-picking*" tool was used to identify "*ID_point*" attribute of points representing green, gray, red, and shadow classes within the point cloud of trees from the reference data set (Figure C1b). The "*ID_point*" attribute was recorded in a spreadsheet and imported into R. The point cloud attributes representing the spectral values and indices of each point were joined with the imported reference data spreadsheet using the "*ID_point*" field. This process resulted in a reference data set of spectral values and indices of points representing green, gray, red, and shadow classes.

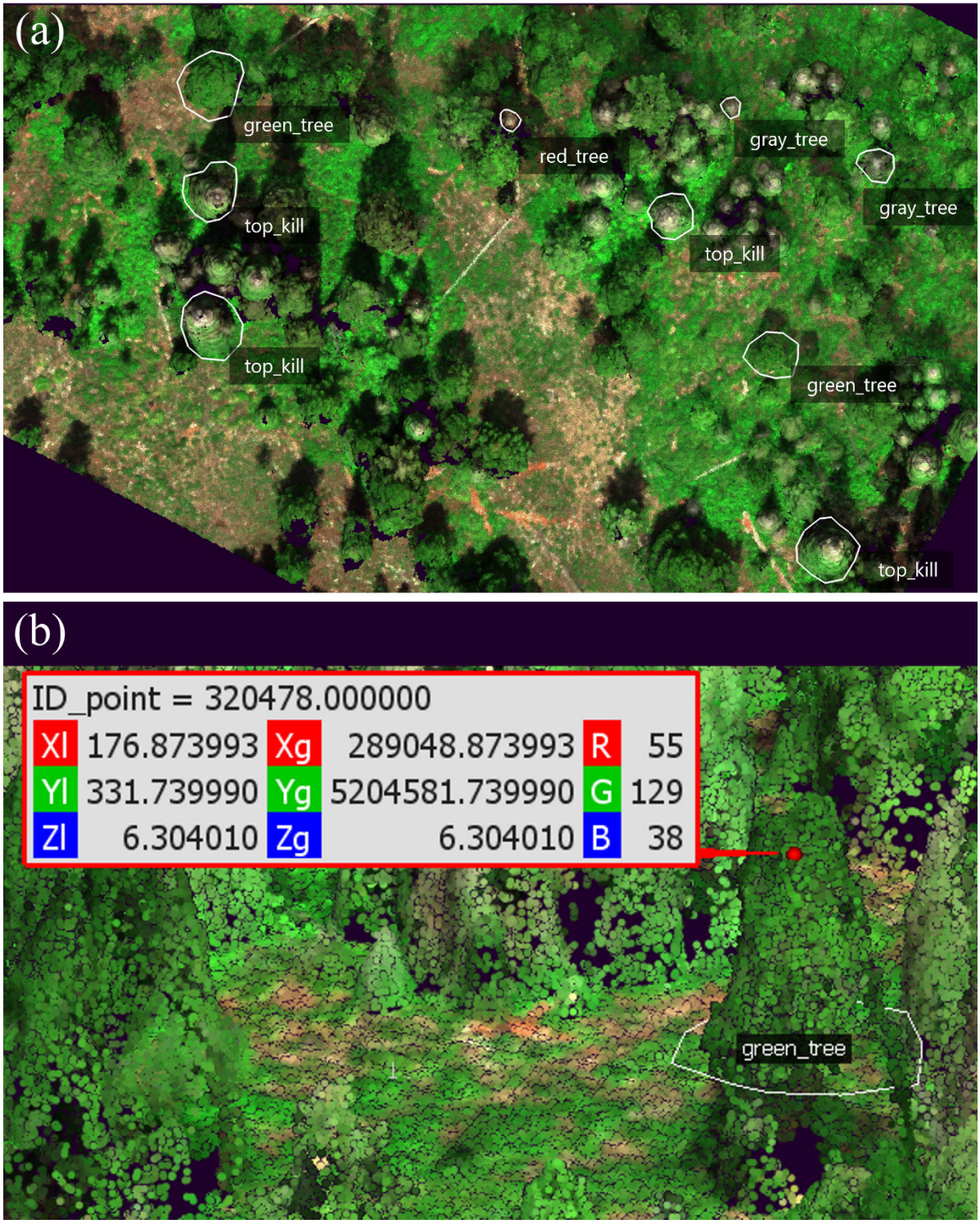

Figure C1. Methods for assembling the reference data set of point clouds using manual point picking in CloudCompare. (a) Top-down view (displayed in CloudCompare) of the subset of the point cloud with the manually identified reference trees (labeled with text). (b) Example of using the "Point-picking" tool in CloudCompare to query the "*ID_point*" of point representing the green class on the reference tree labeled "*green_tree*".

Appendix D. Segmentation of point cloud into trees

D.1. Ground classification and height normalization of point cloud

The ground/non-ground classification and height normalization of the point cloud required for individual tree segmentation followed recommendations from Mohan et al. (2021) and Roussel et al. (2022) using the "*lidR*" R-package (Roussel et al., 2022).

The "*algorithm*" parameter of the "*normalize_height()*" function was set to a K-nearest neighbor with an inverse distance weighting algorithm using the "*knnidw()*" function available in the "*lidR*" package (Roussel et al., 2022). The authors of the "*lidR*" package suggested the "*knnidw()*" algorithm as a suitable compromise between the other two available algorithms (Roussel et al., 2022). These other algorithms are triangular irregular network (TIN) interpolation, which is computationally fast but has weak estimations of edges with prominent edge artifacts, and kriging interpolation which provides the best results in terms of representation of the terrain with minimal edge artifacts but is computationally demanding (Roussel et al., 2022).

D.2. Tree segmentation algorithms

D.2.1. Algorithm background and parameters

The "*lidR*" package consists of various tree segmentation methods that can be broadly categorized into two types: image-based (raster-based) and point cloud-based methods (Roussel et al., 2020). These methods can be used to perform point cloud segmentation of trees.

In image-based tree segmentation methods, the treetops are first detected using a canopy height model (CHM), and the detected treetops are used to segment the point cloud into individual trees (Roussel et al., 2020). The CHM was generated using the "*rasterize_canopy()*" function from the "*lidR*" package (Roussel et al., 2020) and was smoothed using the "*focal()"* function from the "*terra*" package (Hijmans et al., 2023). A majority of drone-based studies in forestry use a fixed window local maximum filtering (LMF) algorithm for tree segmentation (Duarte et al., 2022; Ecke et al., 2022; Guimarães et

al., 2020). Hence for this project, the "*lmf()"* algorithm with the "*locate_trees()"* function from the "*lidR*" package (Roussel et al., 2022) was used for tree segmentation. The "*lmf()"* algorithm parameters for a fixed moving circular window were set to a radius of 1.5 m and a minimum height of 1.35 m. The LMF-located treetop points and the smoothed CHM were used as input for the "*segment_trees()"* function to segment the point cloud into tree segments using the "*silva2016()"* method using the "*lidR*" package (Roussel et al., 2022; Silva et al., 2016). The resulting segmented point cloud consisted of a new attribute, "*treeID*", allocated to every point that is segmented as a tree object, i.e., every point that is segmented as an individual tree will have the same "*treeID*" attribute value (Roussel et al., 2020).

The "*li2012()"* algorithm starts with the highest point in the point cloud data set and applies a proximity search, where, if a second point falls within a radius (set as a parameter), it is considered to belong to the same tree as the first point, and it continues to assess all points that fall within the search radius (Li et al., 2012). The algorithm progresses to the next highest point that falls out of the search radius and considers the outside point as a separate tree and repeats the search radius as with the first tree (Li et al., 2012). All points belonging to an identified tree are allocated the same "*treeID*" attribute (Roussel et al., 2020).

The "*crown_metrics*" function from the "*lidR*" package (Roussel et al., 2022) was used for individual tree crown delineation. The "*geom"* argument for the "*crown_metrics()"* function was set to "*concave*".

D.2.2. Case study to compare tree segmentation algorithms

A preliminary assessment was conducted to determine which tree segmentation algorithm to use for this study. Both tree segmentation algorithms were applied to a subset of the drone mission point cloud and the resulting tree crown polygons were imported in ArcGIS and overlayed on the MS orthomosiac. Qualitative visual assessment and comparisons were conducted to select the better performing tree segmentation algorithm.

The visual assessment of the image-based (Silva et al., 2016) and point cloud-based (Li et al., 2012) segmentation algorithms indicated a better performance by the point cloud-based algorithm (Li et al., 2012). The image-based segmentation algorithm (Silva et al., 2016) had difficulty separating tree crowns in areas of dense forest canopy, failing to detect some of these trees in the subset area (Figure C1a). Conversely, the point cloud-based algorithm (Li et al., 2012) had some errors in dividing a single tree into multiple trees (over-segmentation) (Figure C1b). Correctly detecting trees but with over-segmentation was preferred to failing to detect the presence of trees, and therefore the point cloud-based tree segmentation method (Li et al., 2012) was used here.

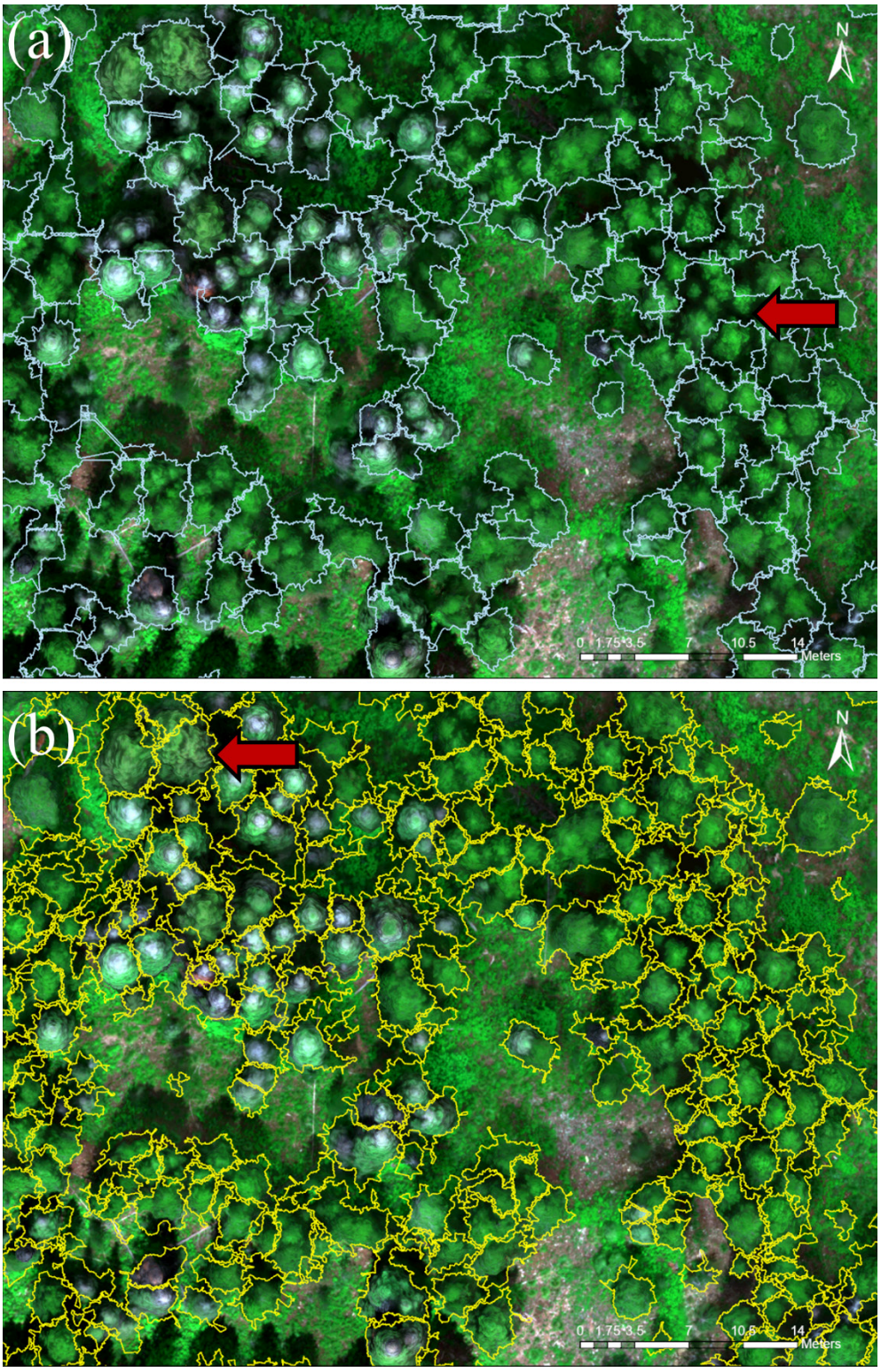

Figure D1. Example of results of tree segmentation. (a) Using the image-based segmentation algorithm (Silva et al., 2016); arrow shows error in detecting trees (no tree detected for area indicated by arrow). (b) Using the point cloud-based segmentation algorithm (Li et al., 2012); arrow shows error of dividing one tree into multiple segments (trees).

D.2.3. Accuracy assessment of tree segmentation

The crowns delineated by the tree segmentation was clipped to a smaller extent to remove the edge artifacts of the drone orthomosaic (Figure 2.1). The "*Create Accuracy Assessment Points*" tool in ArcGIS was used to create randomized assessment points within the clipped extent of the tree segmentation polygon layer. The input information source was set to the tree segmentation polygons layer such that the randomized assessment points inherit the tree segmentation classification results under its "*Classified*" attribute. Randomized points were evaluated with an on-screen assessment to label each point's reference classification under its "*GrndTruth*" attribute. The "*Classified*" attribute of the randomized point cloud represents the predicted class and the "*GrndTruth*" attribute represents the reference class. A total of 1000 randomized points were qualitatively assessed to build the accuracy assessment reference data set. The "*Compute Confusion Matrix*" tool in ArcGIS was used for the accuracy assessment points to produce the confusion matrix and calculate the accuracy metrics.

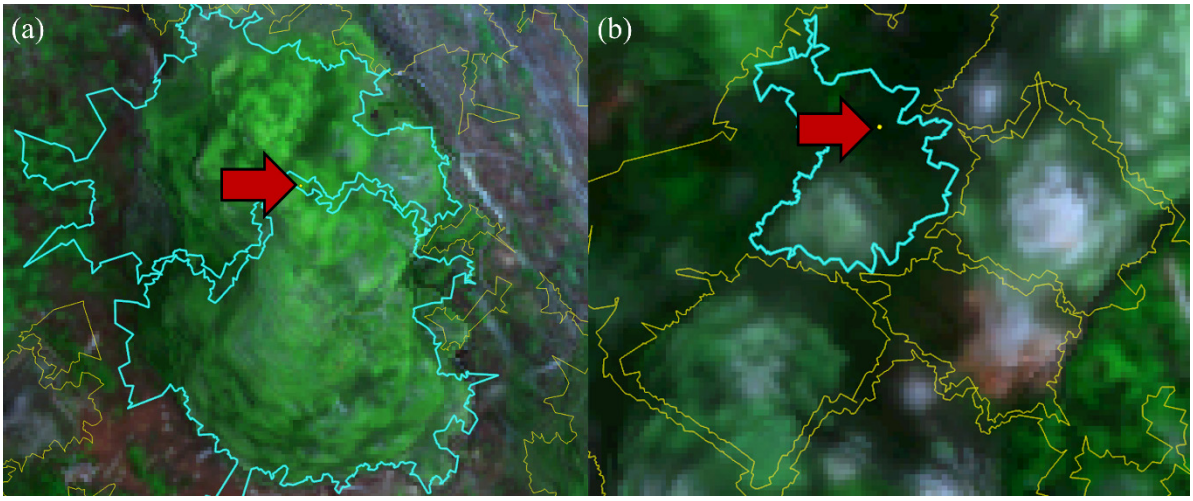

Figure D2. (a) Example from the 352 cases of the "*tree*" class misclassified as the "*not tree*" class (Table 3.1). The accuracy assessment point falls in between the over-segmented tree crown polygons of the tree of interest. (b) Example from the 31 cases of the "*not tree*" class misclassified as "*tree*" class due to tree segmentation issues. The accuracy assessment point falls on ground or understory vegetation but erroneously identified as within the tree crown polygon.

The second accuracy assessment of the tree segmentation was performed using the reference data set of manually delineated tree crowns (100 trees) on ArcGIS. The crowns from the reference data were overlaid with the crowns delineated by the tree segmentation (Figure D3a). The "*Union*" tool was used to separate the overlapping areas of tree crowns from the reference data set and tree segmentation (area *A*, Figure D3b) and the areas that do not overlap (areas *B* and *C*, Figure D3b). The sum of areas *A*, *B*, and *C* were used to calculate the Sørensen's coefficient (SC; (Equation 1)) (Legendre et al., 1998).

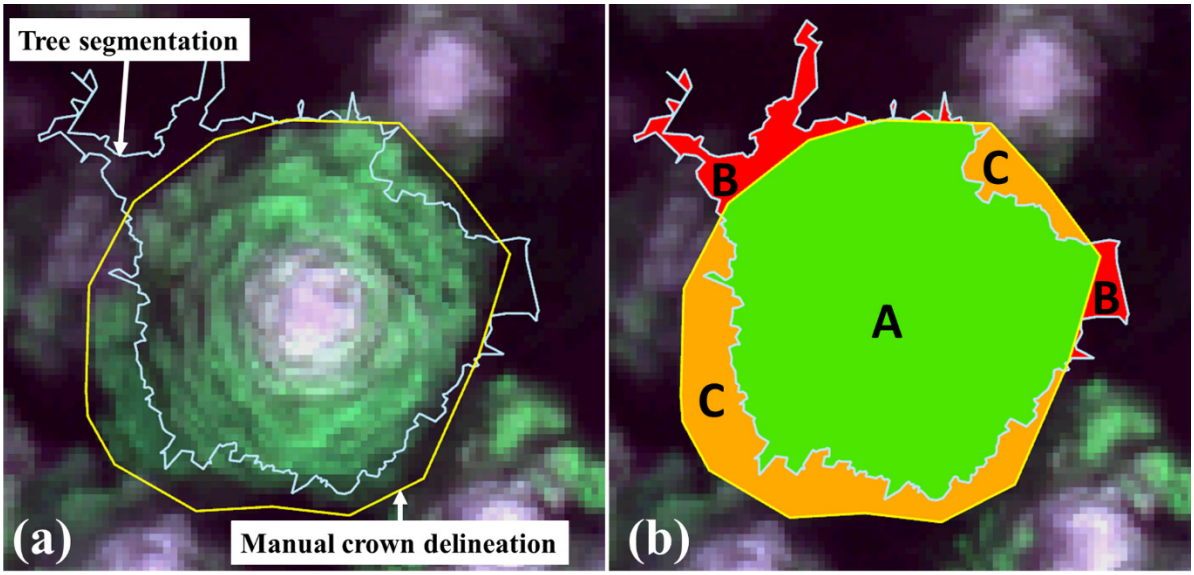

Figure D3. (a) Manually delineated crown polygon (reference data set) overlaid with crown delineation from the tree segmentation algorithm with true color drone orthomosaic as basemap imagery. (b). Segments A, B, and C produced using the "*Union*" tool in ArcGIS with the tree segmentation and manual delineated crowns. "A" is the area identified as tree crown by the manual delineation and the tree segmentation, "B" is area identified as tree crown by the tree segmentation algorithm but not by the manual delineation, and "C" is the area identified as tree crown by the manual delineation but not by the tree segmentation.

Appendix E. Correlation matrix of predictor variables used in RF models.

Figure E1. Correlation matrix of predictor variables used in RF models. The heat map ranging from deep blue to deep red represents the strength of the correlation.

Appendix F. Evaluation of point classification

Table F1. Top five two-variable and three-variable RF models. Maximum pairwise absolute correlation coefficient value ranges from -1 to 1; values approaching -1 indicate strong negative correlation between explanatory variables and values approaching 1 indicate strong positive correlation between explanatory variables.

Rank	Variable	Overall accuracy (%)	Maximum pairwise absolute correlation coefficient (|r|)
two-variable models			
1	RGI + GRE	97.25	0.227
2	RGI + REDEDGE	97.25	0.230
3	RGI + meanRGB	97.25	0.566
4	RGI + BLU	97.00	0.487
5	RGI + NDRE	97.00	0.311
three-variable models			
1	RBI + GLI + GRE	98.75	0.542
2	RBI + NDVI + REDEDGE	98.625	0.389
3	RBI + NDVI + GRE	98.625	0.541
4	RBI + GLI + meanRGB	98.625	0.567
5	RBI + SR + REDEDGE	98.5	0.407

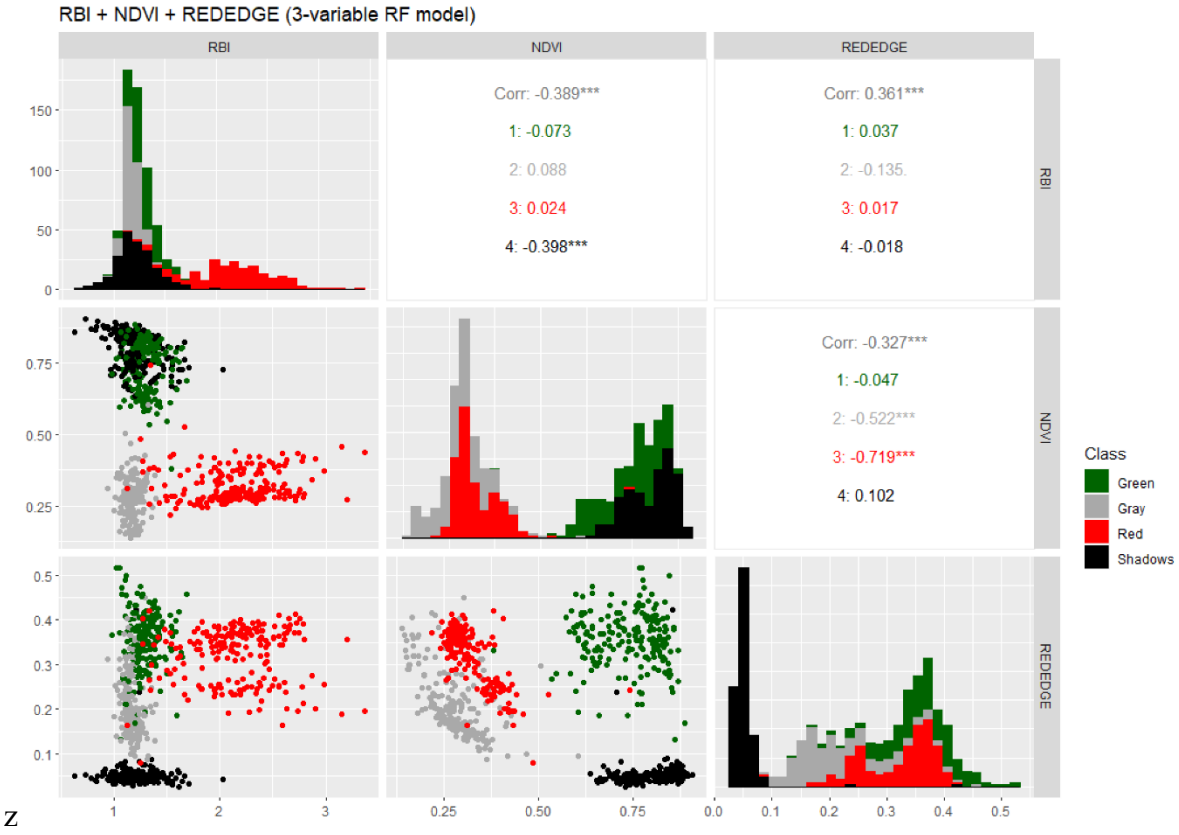

Figure F1. Pairwise plots of predictor variables using reference data set and classes used to develop the final RF model with variables RBI + NDVI + REDEDGE. The diagonal from top-left to bottom-right consists of the histogram of classes for each spectral band and indices. The top-right space above the diagonal consists of correlation values for each of the classes in the respective spectral bands and indices. The bottom-left area below the diagonal consists of a scatterplot of reference data classes with bands and indices plotted on the corresponding axes. The colors of the classes are as labeled on the legend (figure right-hand-side). Figure produced with R function "*ggpairs*" in the "*ggally*" package (Schloerke et al., 2023).

Appendix G. Application of final RF model to point cloud

The "*lidR*" R package stores point cloud data as a "*LAS Class*" R object (Roussel et al., 2022). The attributes of points in the point cloud data were accessed via the "*@data*" slot of the "*LAS Class*" R object (Roussel et al., 2022) and stored as a "*data.table*". A subset "*data.table*" was created which consisted of data from columns representing only the reflectance bands (five bands). The vegetation indices (Table 2.1) were computed and were added as columns to this subset "*data.table*". This "*data.table*" with reflectance bands and vegetation indices was used as the input data to apply the RF model and calculate class probabilities.

The class probabilities for each point, from the final RF model, were calculated using the "*predict()*" function's "*type = prob*" argument (Liaw and Wiener, 2002). The values returned represent the final RF model's classification probability for each point; these values were added as attributes to the point cloud "*data.table*".

The RF model classification and class maximum probabilities were added to the "*LAS Class*" R object using the "*@data*" slot to manually update the attributes of the point cloud object in R. The "*LASheader-class*" is an object in R constructed following ASPRS LAS specifications that helps define the properties and attributes of point cloud object in R and other software that read .las format files (ASPRS, 2019; Roussel et al., 2022). Therefore, the addition of attributes to the point cloud data set required updating the "*LASheader-class*". The "*classify_ground()*" and "*segment_trees()*" functions add attributes to the "*data.table*" of the "*LAS-class*" object in R and automatically updates the "*LASheader-class*" of the point cloud object (Roussel et al., 2022). Manually adding the RF model classification and RF model class probabilities as attributes of each point did not automatically update the "*LASheader-class*". The "*add_lasattribute()*" function was used to update the "*LASheader-class*" with the RF classification attributes and export the classified point cloud as a .las file.

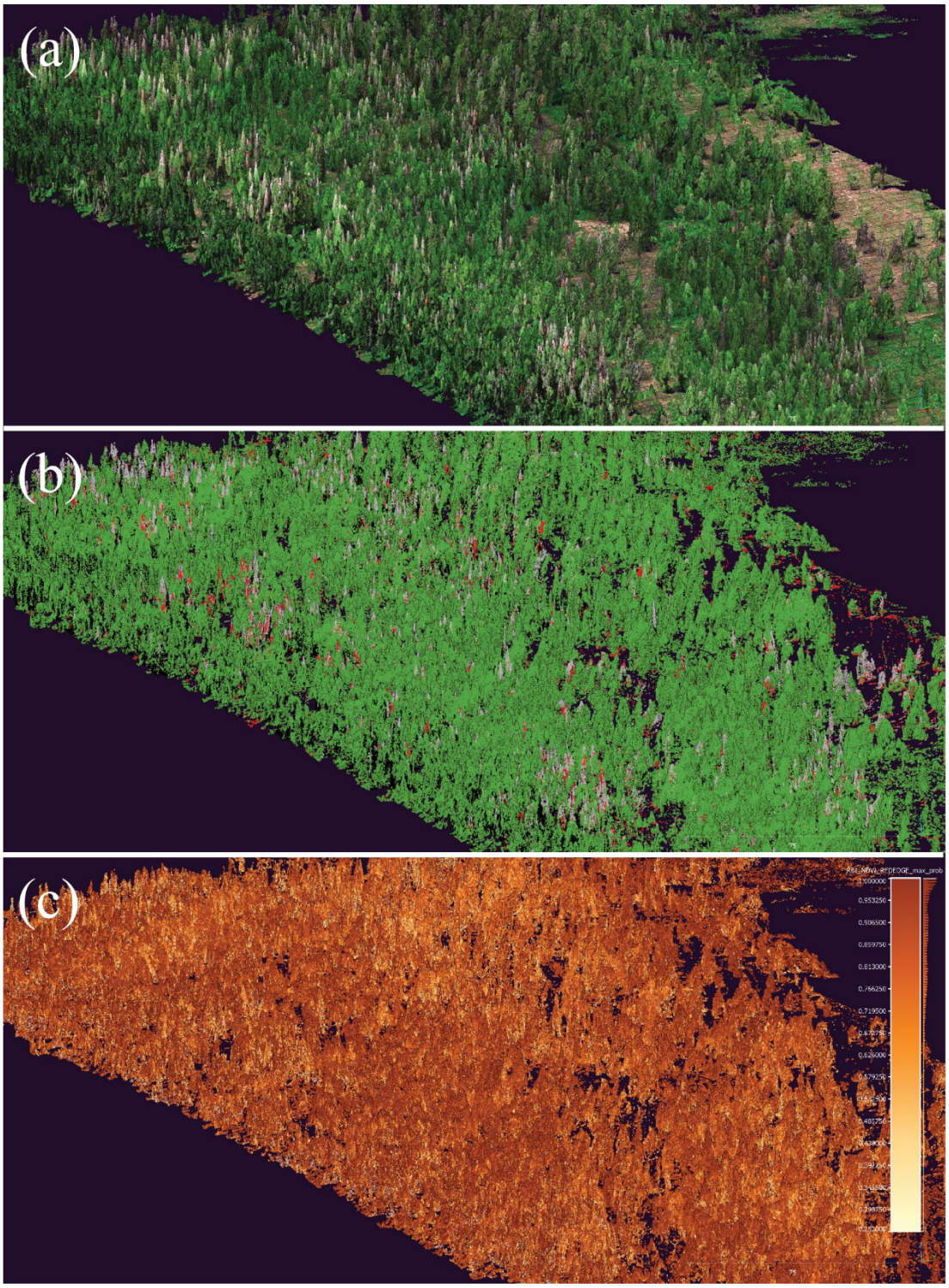

Figure G1. The RBI + NDVI + REDEDGE RF model applied to the point cloud data set for the full extent of the drone site M2. (a) True color rendering of the SfM point cloud for M2. (b) RF classification of SfM point cloud for M2, the colors respond to their respective classes with black used for shadow. (c) Probability for each classified by the RF model, darker brown colors indicate high probability, lighter yellow colors indicate lower probabilities.

Appendix H. Tree-level damage algorithm

H.1. Definition of damage classes

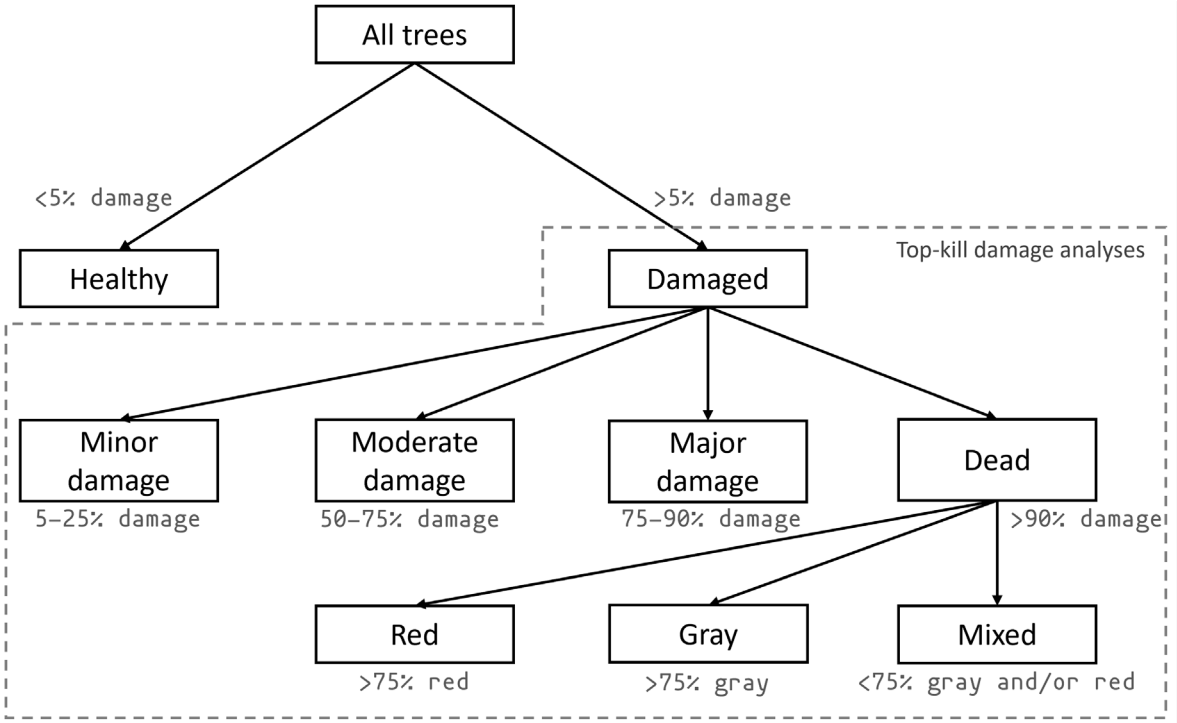

Figure H1. Classification tree used for the separation of trees into healthy, damaged, and different damage types. "Damage" refers to the sum of red and gray points on each tree. The area with dashed line indicates the damage types on which the top-kill algorithms ("t*op2bin*" and "bin2bin") were implemented.

H.2. Preparation of point cloud for damage assessment algorithm

The tree-segmented classified point cloud file was imported into R as a "*LAS Class*" R object to identify damage type of tree using the "*lidR"* package (Roussel et al., 2020). Points classified as ground and shadows were not used in the damage assessment. The ground and shadow points were removed using the "*filter_poi()*" function from the "*lidR"* package (Roussel et al., 2020).

The "*unique()"* function was used to create a list of unique "*treeID*" attributes from the "*@data*" slot of the "*LAS Class*" R object. This list of unique "*treeID*" attributes was used to iterate through individual trees in the imported point cloud data set. The "*filter_poi()"* function from the "*lidR"* package (Roussel et al., 2020) was used to isolate points for individual segmented trees from the imported "*LAS Class*" R object by setting the "*treeID ==*" argument to the elements of the unique "*treeID*" list. The damage analysis only requires the height and classification information, and therefore only the "*Z*" and classification columns were extracted from the filtered point cloud data set's "*@data*" slot and stored as a "*data.table*" for the tree-filtered point cloud data set. Performing damage assessment on the "*data.table*" with only two columns is more efficient than using the "*LAS Class*" R object with multiple columns and data slots, especially for iterative operations.

H.3. Types of tree-level damage algorithms

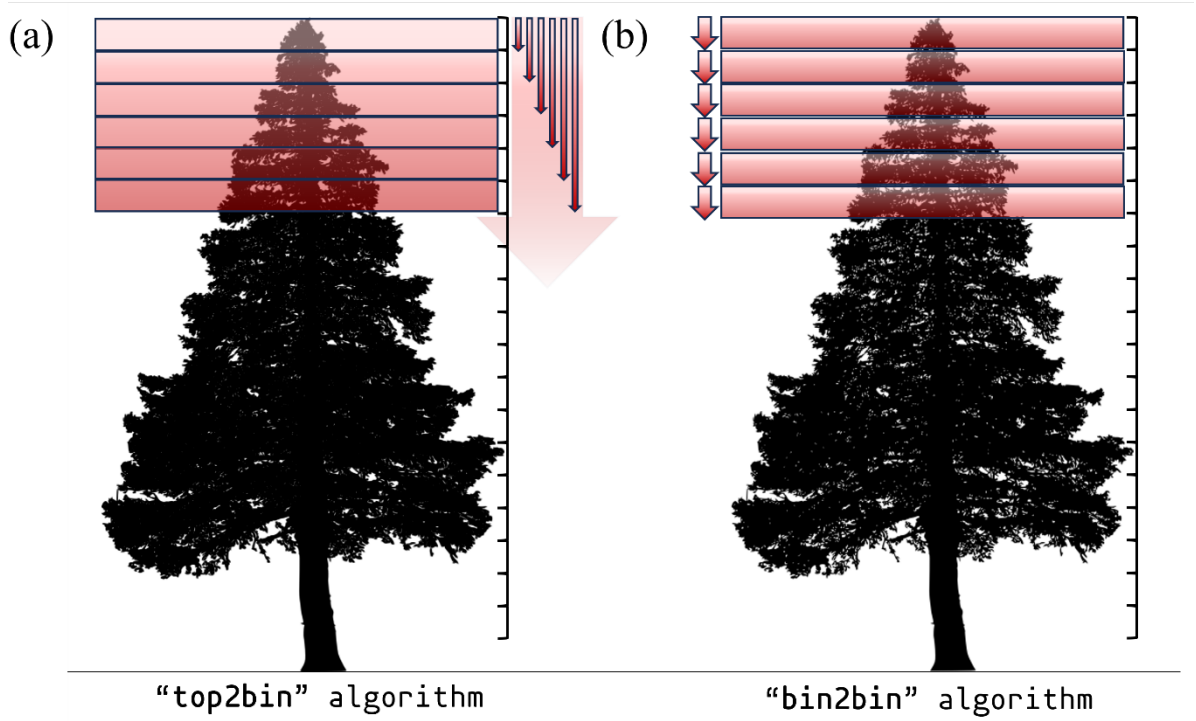

Figure H2. (a) The *"top2bin"* algorithm assesses the percentage of damage classified points within an increment defined for height bins from the top of the tree to a given height beginning at the top of the tree and moving downward. For example, if the tree is 10 m tall, the "*top2bin*" algorithm assesses damage from 10 m above ground to 9.75 m above ground (0.25 m bin) for the first increment (consisting of one bin), and then assesses damage from 10 m above ground to 9.5 m above ground for the second increment (consisting of two bins). The algorithm halts when the percentage of damaged points within an increment is below a threshold. (b) The *"bin2bin"* algorithm assesses the percentage of damage classified points for each height bin beginning at the top of the tree and moving downward. For example, if the tree is 10 m tall, the "*bin2bin*" algorithm assesses damage from 10 m above ground to 9.75 m above ground for the first bin, and then assesses damage from 9.75 m above ground to 9.5 m above ground for the second bin. The algorithm halts when the percentage of damaged points within a bin is below a threshold.

H.4. Accuracy assessment of tree-level damage algorithm

The tree polygons with tree-level damage analysis information were imported into ArcGIS and the polygon layer was clipped to a smaller extent to remove the edge artifacts of the MS and RGB orthomosaics.

The "*Create Accuracy Assessment Points*" tool in ArcGIS was used to create stratified random assessment points within the clipped extent. The input information source was set to the tree damage assessment polygon layer such that the randomized assessment points inherit the damage type classification results under its "*Classified*" attribute. Randomized points were evaluated with an on-screen assessment in which each point's reference classification was recorded as its "*GrndTruth*" attribute. The MS and RGB orthomosaics were used as the primary source of visual assessment, and individual drone-captured images were consulted for cases that needed additional information. A total of 1000 randomized points were qualitatively assessed to build the accuracy assessment reference data set.

The "*Compute Confusion Matrix*" tool in ArcGIS was used on the accuracy assessment points to produce the confusion matrix and calculate the accuracy metrics. The confusion matrix from the accuracy assessment on ArcGIS consisted of substantial class imbalances with most of the accuracy assessment points falling in the "healthy" class. To address this class imbalance, the attribute table of the accuracy assessment points was imported in R and a bootstrap sampling method was implemented to produce an averaged confusion matrix and computed accuracy metrics (Hardin and Shumway, 1997).

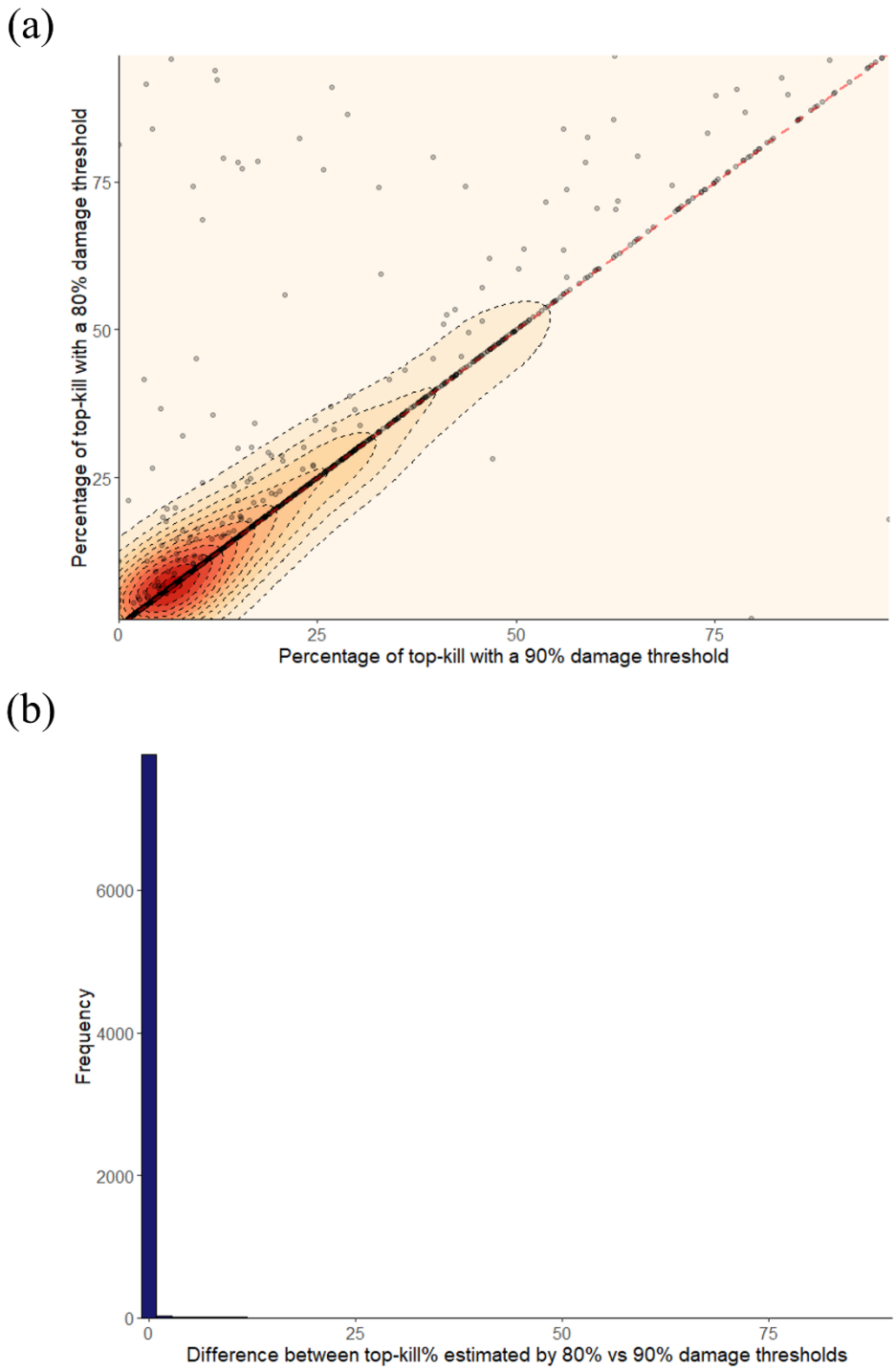

Figure H3. (a) Percent top-kill estimated with a 90% damage threshold with the "*top2bin" algorithm* versus percent top-kill estimated with an 80% damage threshold with the "*bin2bin"* algorithm on the point cloud of study area. Contour lines and color ramp show the density data points, most of which fall along the 1:1 line. (b) Frequency histogram of difference in percent top-kill estimated by a 90% damage threshold and 80% damage threshold. High frequency of 0 values indicates minimal difference.

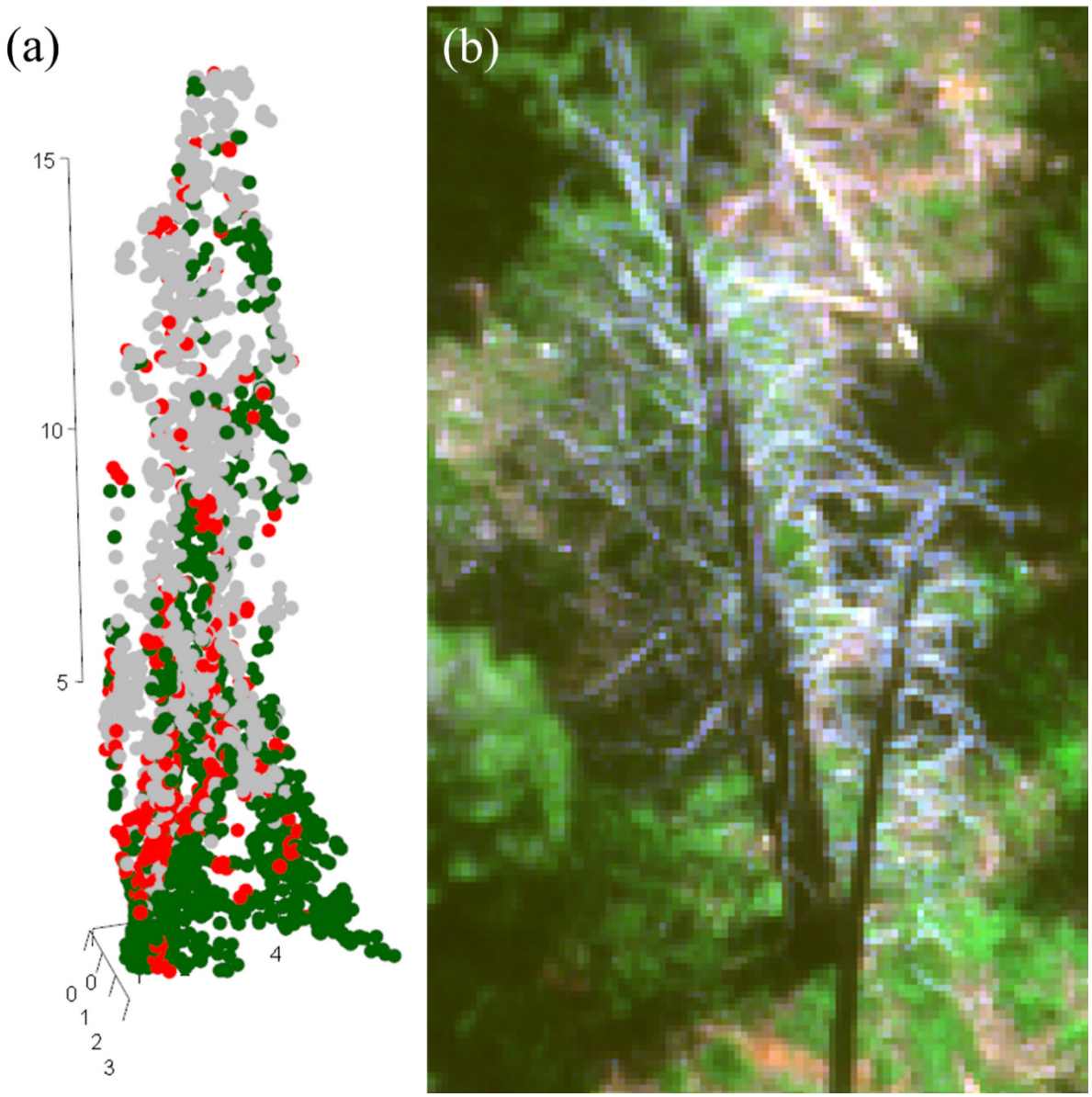

Figure H4. (a) Point cloud of a "*Dead*" tree from the reference data set with green classified points on the bottom and middle. (b) Oblique view of the true color image of the "*Dead*" tree in (a).

H.5. Live crown base issue with SfM point clouds

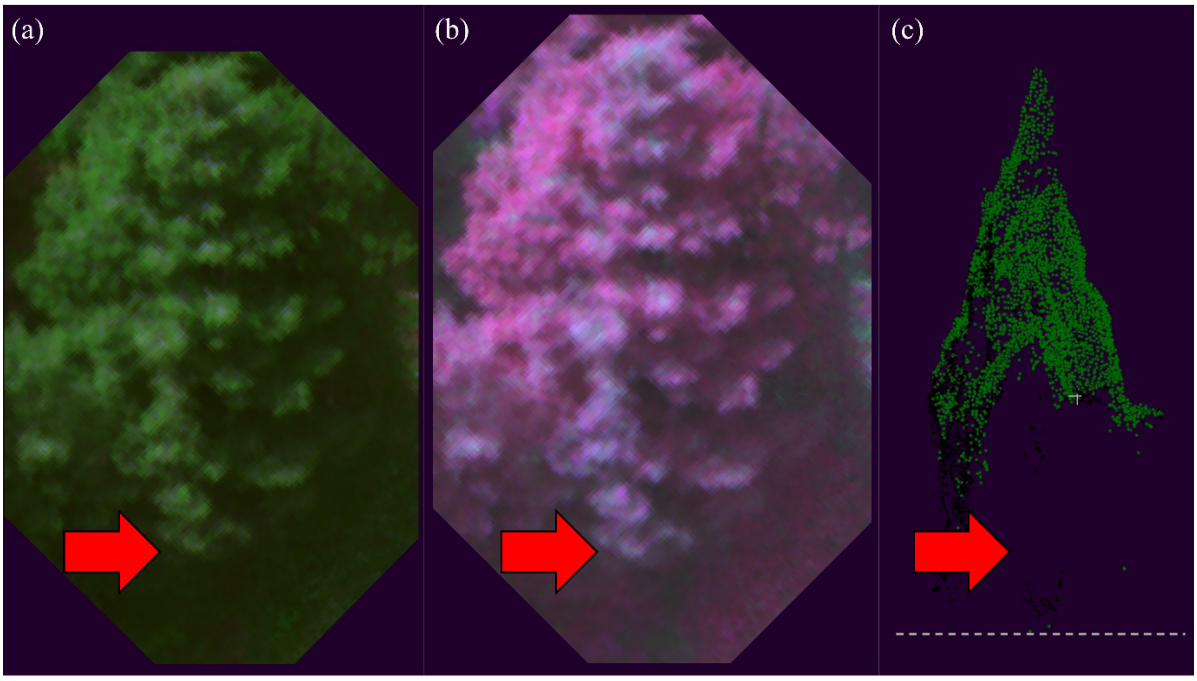

Figure H5. (a) True color and (b) false color drone images of an example tree with live crown base above ground (red arrows indicate live crown base). (c) SfM point cloud of the example tree in (a) and (b); red arrow on SfM point cloud shows absence of points providing inconclusive information for live crown base estimation; gray dashed line represents ground. The orientation of the point cloud in (c) was adjusted to match the view of the tree in (a) and (b). The placement of the red arrows was an estimation of where the points representing the crown base should be based on the orientation.